Bahrami and Rosen *Geothermal Energy* (2024) 12:12
https://doi.org/10.1186/s40517-024-00293-7

Geothermal Energy

RESEARCH Open Access

Exergoeconomic evaluation and multi-objective optimization of a novel geothermal-driven zero-emission system for cooling, electricity, and hydrogen production: capable of working with low-temperature resources

Hamid-Reza Bahrami[1*] and Marc A. Rosen[2]

*Correspondence: taleshbahrami@qut.ac.ir; h_tbahrami@yahoo.com

[1] Department of Mechanical Engineering, Qom University of Technology, P.O. Box 37195-1519, Qom, Iran
[2] Faculty of Engineering and Applied Science, Ontario Tech University, 2000 Simcoe Street North, Oshawa, ON L1G 0C5, Canada

Abstract

Geothermal energy is an abundant natural resource in many regions around the world. However, in some areas, the temperature of the geothermal energy resource is too low to be efficiently harvested. Organic Rankine cycles (ORCs) are known for recovering heat from low-temperature resources and generating electricity. Furthermore, half-effect absorption chillers (HEACs) are designed to produce cooling with low-temperature resources. This study proposes a novel configuration that utilizes an ORC for electricity generation, a HEAC for cooling production, and a PEM electrolysis system to produce hydrogen. The power section consists of two turbines, one driven by the vapor produced from the geothermal flow expansion, which powers the PEM section, while the other turbine in the ORC is used to drive pumps and electricity production. First, the system is thermoeconomically analyzed for an initial set of inputs. Then, various parameters are analyzed to determine their influences on system performance. The analyses reveal that the system can work with geothermal source temperatures as low as 80 °C, but the exergy and energy (thermal) efficiencies decrease to around 17% under the base settings. Furthermore, the system is capable of working with resource temperatures up to 170 °C. Ten parameters are found to affect the system's efficiency and effectiveness. To optimize the system, the Non-dominated Sorting Genetic Algorithm II (NSGA-II) is implemented to find the optimum conditions. The objective functions are exergy efficiency and unit polygeneration cost (UPGC), which can conflict. The optimization shows that the exergy efficiency of the system can reach 48% in the optimal conditions (for a heat source temperature of 112 °C and a mass flow rate of geothermal fluid of 44 kg/s), with a hydrogen production rate of 1.1 kg/h.

Keywords: Hydrogen production, Absorption refrigeration, Geothermal energy, Multigeneration, Half-effect absorption chiller

Springer Open

© The Author(s) 2024. **Open Access** This article is licensed under a Creative Commons Attribution 4.0 International License, which permits use, sharing, adaptation, distribution and reproduction in any medium or format, as long as you give appropriate credit to the original author(s) and the source, provide a link to the Creative Commons licence, and indicate if changes were made. The images or other third party material in this article are included in the article's Creative Commons licence, unless indicated otherwise in a credit line to the material. If material is not included in the article's Creative Commons licence and your intended use is not permitted by statutory regulation or exceeds the permitted use, you will need to obtain permission directly from the copyright holder. To view a copy of this licence, visit http://creativecommons.org/licenses/by/4.0/.

Introduction

The rising global demand for energy and concerns over greenhouse gas emissions have shifted attention towards renewable energy sources, such as biomass, solar, wind, and geothermal, aiming to reduce reliance on fossil fuels. In many locations around the world, low-temperature geothermal resources (less than 125 °C) are available, which are usually used directly in applications such as greenhouse heating, space heating, or aquaculture (Putriyana et al. 2022). Using these resources more effectively to produce power is important, but it may not be attractive economically. Therefore, incorporating additional subsystems, such as cooling and/or hydrogen production, becomes beneficial to enhance the revenue portfolio and improve the cost-effectiveness of geothermal energy. For example, in remote areas where power transmission lines are not accessible, the generated power can be used for hydrogen production. Alternatively, a portion of the electricity can be sold to the local grid, while the remaining power is dedicated to hydrogen production. Furthermore, waste heat, which cannot be effectively utilized for power production, can be harnessed for cooling purposes, such as in cold storage facilities. Moreover, seasonally, part or all of the integrated system can be utilized based on seasonal demands in the market.

Recent studies have focused extensively on multigeneration systems that produce hydrogen and oxygen (Zhang et al. 2023). These systems can be combined with several energy technologies, such as combined power and cooling (Aryanfar and Alcaraz 2023; Blanke et al. 2021; Huang et al. 2023; Tang et al. 2022; Wang et al. 2019), power and heating (Marefati et al. 2019; Wu et al. 2019), and heating, cooling, and power (Assareh et al. 2023; Pang et al. 2023).

Numerous studies have been reported recently in these areas, highlighting their importance. Delpisheh et al. (2021) proposed a solar-based setup to produce freshwater, electricity, and hydrogen from seawater. It uses solar collectors, an organic Rankine cycle (ORC) for electricity, a low-temperature electrolyzer for producing hydrogen, and a desalination unit for freshwater. The cost per unit exergy was determined for different solar radiation modes: 80 $/GJ for low radiation, 60.3 $/GJ for high radiation, and 81.4 $/GJ for no radiation. While this system has good energy efficiency in basic design mode (81.46%), it has low exergy efficiency (5.22%). Karabuga et al. (2023) examined a solar–ORC system combined with a heat pipe solar collector to produce hydrogen. The modified system attained exergy and energy efficiencies of 2.15% and 3.45%, respectively, when all electricity was used for hydrogen production. Nevertheless, the exergy and energy efficiencies of the proposed system are not high which implies that the system may face challenges in practical implementations. Farajollahi et al. (2023) introduced a new system to recover unused heat using a dual-flash binary geothermal power generation plant to enhance overall efficiency. The system optimizes energy usage by incorporating reverse osmosis desalination, a Rankine cycle, and a proton exchange membrane electrolyzer (PEME). Using a non-dominated sorting genetic algorithm-II (NSGA-II) technique, the system achieves an average cost of products of 4.54 $/MWh and an exergy efficiency of 43.83%. The estimated freshwater production rate, net output power, and hydrogen production rate, respectively, are 22.51 kg/s, 6474 kW, and 1.84 kg/h. The drawbacks of this system pertain primarily to reverse osmosis freshwater production. The quality of the output water is dependent on the conditions of the inlet water and the

quality of the membranes, which deteriorate over time as the system operates. Razmi et al. (2023) introduced a hybrid approach using solid oxide electrolyzer/fuel cells and a heliostat solar field to generate green hydrogen using advanced high-temperature units. The system can generate electric power at as high a rate as 54.3 MWh and achieves a hydrogen production rate of 7.76 tons/day, with an overall efficiency of 74.2%. However, the heliostat field needs a large land area, which may negatively affect ecosystems and wildlife habitats either because of the removal of flora to create bare land for installing mirrors or due to unwanted reflected beams affecting neighborhoods. Wang et al. (2023) examined a hybrid system that combines wind turbines with a biomass-driven SOFC to improve hydrogen concentration in the fuel. Feasibility studies and performance evaluations show significant efficiency enhancement, with increasing wind power leading to higher net power and efficiency. The optimal point yields a net output power of 322 kW. However, the sustainability and environmental effects of biomass and the intermittent nature of wind energy are drawbacks of the mentioned renewable energy resources. Yuksel et al. (2023) designed a geothermal-based multigeneration plant, including a Kalina cycle, freshwater production, liquid hydrogen production, and a thermoelectric generator. The system achieves energy and exergy efficiencies of 46.87% and 44.13%, respectively. The maximum exergy destruction happens in the Kalina cycle, while liquid hydrogen production exhibits the highest exergy efficiency of 54.17%. Eight key factors influencing the system's efficiency are evaluated. Khodaparast et al. (2023) investigated efficient configurations for systems to liquefy hydrogen, combining a geothermal-driven ORC and a Claude cycle to reduce compression work and enhance liquid nitrogen supply. A thermoeconomic assessment was conducted, highlighting the significance of combined modeling for liquid nitrogen supply in achieving better system performance under various conditions.

Geothermal energy is an important renewable resource due to its reliability, stability, and relatively widespread accessibility (Zare and Takleh 2020). This form of energy includes the heat stored underground over a wide temperature range. Combining geothermal sources and absorption chillers has been extensively considered for multigeneration. For instance, Hai et al. (2023) proposed an integrated energy system that produces electricity, potable water, heating, cooling, and H_2. It was evaluated using various indicators and subject to optimization. The system produces 99.25 kW of output work and has exergy and energy efficiencies of 32.1% and 24.4%, respectively. This study reveals that increasing the geothermal flow temperature reduces the values of the exergoenvironmental parameters while increasing the pressure of FT1 increases cooling load and energy efficiency but decreases other factors. Zhang et al. (2022) studied a parallel double-effect absorption power cycle based on LiBr–water brine to utilize effectively geothermal energy utilization. The system improves exergy efficiency by 12.3% and net power output by 41.3% and reduces total product unit cost by around 10.1%. However, the study lacks an optimization process which may provide better results. Li et al. (2022) introduced a trigeneration layout featuring a cascade electricity production system, PEME, and a CO_2 compression refrigeration system with an absorption refrigeration system (ARS) after-cooler. The system was enhanced thermodynamically to maximize its efficiency and effectiveness, resulting in an exergy efficiency of 26.5%. At the optimum conditions, the system generates 451.8 kW of net output power, provides a cooling

rate of 297.8 kW, and produces hydrogen at a rate of 2.274 kg/h, combining absorption and compression technologies.

Single-effect absorption cycle elements are highly interdependent, meaning that the heat sink, source, and generator temperatures are dependent (Schweigler et al. 1999). The mentioned temperature constraint can be overcome using a half-effect absorption chiller (HEAC), also known as a double-lift cycle, which allows for a broader range of cooling water temperatures (Herold et al. 2016). Half-effect absorption chillers can work at lower temperature ranges, as low as 80 °C (Loreti et al. 2019), although their exergy efficiency and coefficient of performance may be lower than that of higher-effect absorption chillers when used with higher temperature sources (Maryami and Dehghan 2017). Domínguez-Inzunza et al. (2014) assessed various arrangements of absorption cooling chillers. The half-effect system has advantages, including lower generation temperatures (starting from 55 °C) and better performance at high condensation and absorption temperatures (up to 40 °C). However, its coefficient of performance is roughly half that of single-effect systems. Hernández-Magallanes et al. (2019) performed a thermodynamic assessment on a cooling system that utilizes a low-enthalpy geothermal source and operates based on a half-effect absorption mechanism. The system used an $NH_3/LiNO_3$ mixture and achieved cooling temperatures as low as −16 °C, with a COP between 0.10 to 0.36 and exergy efficiency varying between 0.15 and 0.40. The proposed system operated within a temperature range of 56 to 70 °C using real data from geothermal wells in Baja California Sur, Mexico. Chen et al. (2019) evaluated and compared the thermoeconomic performances of four dissimilar solar trigeneration systems based on photovoltaic thermal (PVT) collectors coupled with single-effect and half-effect refrigeration chillers. The results show that the configuration based on glazed PVT collectors joined with HEAC performs the best, achieving the maximum solar COP and solar utilization factor. Chen et al. (2019) highlight the potential of using HEAC to improve solar multigeneration system performance relying on PVT collectors in subtropical climates.

In summary, it can be seen that although geothermal energy is a reliable resource, it usually has low exergy values, which makes it challenging to exploit efficiently. That is, geothermal resources usually have low temperatures, making harvesting difficult. The literature also confirms that the energy efficiency of geothermal systems is not very high. However, it should be noted that although the efficiency of these systems may be low, the denominator of the efficiency ratio is almost free, unlike systems that rely on fossil fuels. Nevertheless, exergy efficiency is important because it refers to the capability to extract the maximum available or useful energy from a resource. This study aims to propose a system that can efficiently utilize low-temperature geothermal resources and analyze them to enhance understanding. The current investigation proposes and assesses a combined system that utilizes an ORC, a HEAC, and a PEM electrolyzer to harvest energy from geothermal resources with an acceptable polygeneration cost. The purposeful integration of the HEAC within the system enables it to work effectively with low-temperature resources. After evaluating the system under initial settings, a parametric investigation is carried out to identify the system performance with different values of parameters. In the next step, a multi-objective optimization is applied to find the

system's optimal performance. Finally, the system's effectiveness is compared with other proposed configurations in the literature.

System description and assumptions

An innovative layout is proposed in this study to exploit geothermal energy to generate cooling, electricity, and hydrogen simultaneously. A single-flash geothermal power cycle linked with an organic Rankine cycle is used in the power section. This section has two turbines. The power produced by one turbine (driven by geothermal fluid vapor produced in the flash process) is completely used for the electrolysis process. The power of the other turbine (driven by the ORC) is used to drive pumps, and the rest is net output power. The geothermal fluid is then used in a half-effect cycle as the heat source to generate cooling. In the next stage, the geothermal fluid is collected, and part of it is used to preheat the water needed for the electrolysis process using a proton exchange membrane electrolyzer. Note in particular that including the HEAC in this system is crucial for working with low-temperature resources. In some situations, the temperature of the geothermal fluid following the geothermal power cycle drops considerably, rendering the utilization of single/multiple effects absorption chillers impractical. Moreover, the ORC is employed to harness considerable thermal energy from the liquid part of the geothermal flow after the expansion.

It is noted that, prior to this study, the feasibility of various configurations (including all/some mentioned subsystems) was assessed through multiple thermodynamics analyses based on the first and second laws, leading to the adoption of the specific configuration presented here.

Details of the proposed system for cooling, electricity, and hydrogen are depicted in Fig. 1. The plant incorporates three subsystems: an ORC, a HEAC working by water–lithium bromide, and a PEME. The hot geothermal fluid enters the system via line 7 and undergoes expansion through Ex.1 before entering a separation tank. The tank separates the geothermal fluid into vapor and liquid phases, each following its designated path. The vapor phase proceeds to turbine 1, where it expands and generates power. It then is conveyed to the low-pressure generator (LPG) of HEAC, transferring its remaining useful energy to the LPG. Simultaneously, the liquid phase from the separation tank, line 9, is conveyed to the ORC. In this stage, the liquid exchanges some of its remaining useful energy through HEX 1 to the ORC. Flow 10 remains hot. Next, it is directed towards the high-pressure generator (HPG) of the HEAC, where additional energy transfer occurs. The flow from line 14 subsequently merges with another portion of the geothermal fluid from line 13. A fraction of the combined flow is diverted through line 16 to preheat the input water for the PEME section, which enters at ambient temperature. Subsequently, it exits HEX4 at position 18 and rejoins the main part of the geothermal fluid, ultimately returning to the geothermal well at 19. The ORC maintains a specific pressure at HEX 1, which creates a consistent temperature difference with the geothermal fluid at line 9. This produces superheated vapor at line 4 that powers turbine 2 to generate work. The vapor then enters condenser 1, condenses, and is compressed by pump 1 to the specified pressure. In the HEAC section, the weak brine (LiBr–water) arrives at the LPG (low-pressure generator), which is heated by geothermal fluid, producing water vapor. The vapor comes in the high-pressure absorber (HPA), while the strong solution returns to the low-pressure absorber (LPA). Before entering the

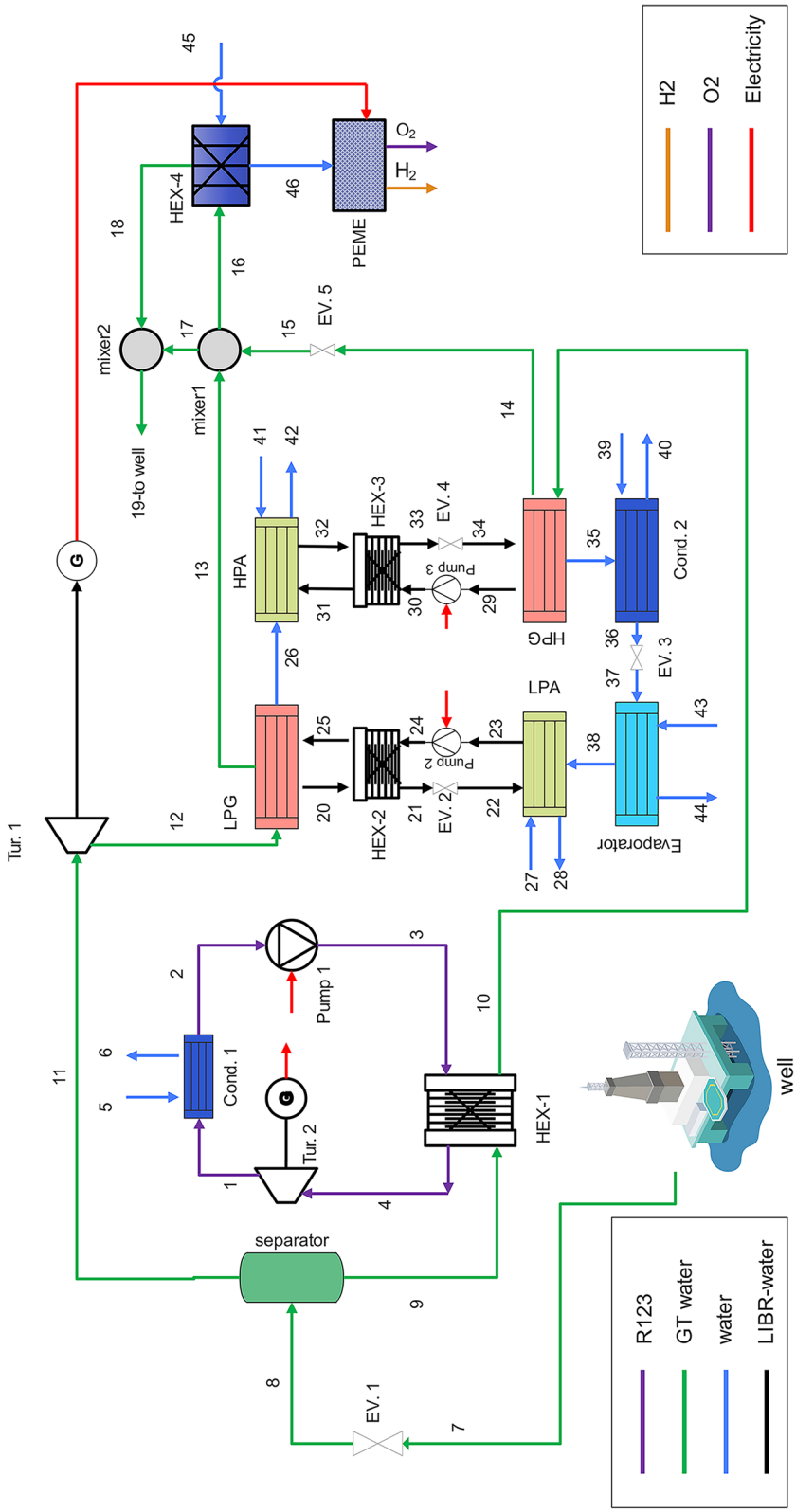

Fig. 1 Schematic of the designed multigeneration system (Tur.: turbine, HEX: heat exchanger, Cond.: condenser, EV: expansion valve, GT: geothermal)

expansion valve (EV. 2), the strong solution exchanges energy with the cooler weak solution that exits the pump. After expanding, the strong solution enters the LPA. External low-temperature water flow also helps to cool the brine and absorb water vapor from line 38. Once enough water has been absorbed, the brine is pressurized to a higher pressure and directed toward the high-pressure generator (HPG) in line 23. As mentioned before, the vapor produced in the LPG enters the HPA via line 26. The HPA absorbs it via the strong solution from the HPG in line 31. The other parts of the high-pressure section are similar to the low-pressure section, except for the vapor produced in the HPG. This vapor is directed towards condenser 2 (Cond. 2), where it is condensed. After passing through an expansion valve, its pressure reduces, providing cooling in the evaporator. In the hydrogen production section, preheated water is passed to the PEME, where the power produced by turbine #1 is utilized to split water into oxygen and hydrogen.

The present simulation and analysis employs several assumptions to manage its complexity:

- The investigation is done under steady-state and thermodynamic equilibrium conditions.
- The surroundings are taken to be at a pressure of 101.3 kPa and a temperature of 25 °C.
- All compressors, turbines, and pumps operate adiabatically with assumed isentropic efficiencies.
- Negligible variations are present in potential and kinetic energies.
- The condenser's output flow is assumed to be completely condensed, while the evaporator's output is supposed to be saturated vapor.
- It is assumed that the solutions in the absorbers and the generators are in equilibrium.
- The water–lithium bromide solution that exits the absorber or generator is diluted at the same temperature as the absorber or generator.

Boundary conditions and input information for the system are given in Table 1. Subsequently, the system's sensitivity to some of these parameters is analyzed, and optimization is performed to ensure that the parameters are appropriately selected.

Energy and exergy analysis

In the current investigation, the first law of thermodynamics was utilized to describe the overall energy conservation of the system. Relying on the mentioned assumptions, a general energy rate balance for an element could be written as follows (Bahrami and Fazli 2024):

$$\dot{Q} + \sum_k (\dot{m}_{\text{in}} h_{\text{in}})_k = \dot{W} + \sum_k (\dot{m}_{\text{out}} h_{\text{out}})_k, \tag{1}$$

where $\dot{Q}$ and $\dot{\text{W}}$ are heat and work rates, respectively, which cross boundaries.

Additionally, a general exergy rate balance for each component can be written as follows (Mohseni et al. 2024):

$$\dot{\text{E}}\text{x}_{\text{heat}} + \sum_k \left(\dot{\text{E}}\text{x}_{\text{mass,in}}\right)_k = \dot{\text{E}}\text{x}_{\text{work}} + \sum_k \left(\dot{\text{E}}\text{x}_{\text{mass,out}}\right)_k + \dot{\text{E}}\text{x}_d, \tag{2}$$

where

Table 1 Input information for simulating the multigeneration system

Parameter	Value
Environmental pressure, P_0 (kPa)	100
Environmental temperature, T_0 (°C)	25
Geothermal fluid mass flow rate, $\dot{m}_7$ (kg/s)	10
Geothermal water temperature, T_7 (°C)	150
Geothermal water pressure (kPa)	266
Condenser 1 temperature (°C)	30
$\Delta T_{HEX1} = T_9 - T_4$ (°C)	27.4
Turbine 1 outlet pressure, P_{12} (kPa)	30
HEX 1 temperature (°C)	100
Maintenance factor, φ_r (–)	1.06
System lifetime, N (years)	20
Interest rate, I_r (%)	10
Annual operation hours, τ (h)	7446
Separator pressure (kPa)	250
Anode activation energy, $E_{act\,a}$ (kJ/kg)	76
Cathode activation energy, $E_{act\,c}$ (kJ/kg)	18
λ_c (1/Ω)	10
λ_a (1/Ω)	14
Thickness of membrane, D (μm)	100
Anode pre-exponential factor, J^a_{ref} (A/m^2)	1.7×10^5
Cathode pre-exponential factor, J^c_{ref} (A/m^2)	4.6×10^3
Faraday constant, f (C/mol)	96,486
Geothermal exergy unit cost ($/GJ)	1.3
Geothermal fluid	Water
Organic Rankine fluid	R123
HPA pressure (kPa)	$(P_{HPG} + P_{LPG})/2$
HPG temperature (°C)	T_{10}–5
Low-pressure generator temperature (°C)	T_{12}–5
Evaporator temperature (°C)	5
T_6–T_5 (°C)	5
$\Delta T_{Cond.1} = T_2 - T$ (°C)	5
$\Delta T_{Cond.2} = T_{36} - T_{40}$ (°C)	5
T_{10}–T_{29} (°C)	5
T_{12}–T_{13} (°C)	5
T_{12}–T_{20} (°C)	5
T_{28}–I_{27} (°C)	5
T_{23}–T_{28} (°C)	5
T_{42}–T_{41} (°C)	5
$\Delta T_{HPA} = T_{32} - T_{41}$ (°C)	5
$\Delta T_{HS} = T_7 - T_8$ (°C)	20.45
T_{40}–T_{39} (°C)	5
T_{43}–T_{38} (°C)	5
T_{16}–T_{18} (°C)	5
T_5, T_{27}, T_{42}, T_{39}, T_{43}, T_{41} (°C)	25
ε_{HEX}	0.75
η_{tur}	0.85
η_p	0.85

$$\dot{\mathrm{E}}\mathrm{x}_{\mathrm{mass},k} = \dot{m}_k((h_k - h_0) - T_0(s_k - s_0) + \mathrm{ex}_{\mathrm{ch}}) \tag{3}$$

and

$$\dot{\mathrm{E}}\mathrm{x}_{\mathrm{work}} = \dot{W} \tag{4}$$

Table 2 provides exergy and energy rate balances for each system component, enabling a comprehensive assessment of the system's effectiveness and performance.

The proposed multigeneration system aims to produce hydrogen, power, and cooling, utilizing hot geothermal water as its energy source. This system's energy (or thermal) efficiency is determined by calculating the sum of the net produced power, stored hydrogen, and cooling effect, and dividing by the input energy derived from geothermal hot water. That is:

$$\eta_t = \frac{\dot{W}_{\mathrm{tur2}} + \dot{Q}_{\mathrm{ev}} + \dot{m}_{H_2}\mathrm{LHV}_{H_2}}{\dot{Q}_{\mathrm{geo}}}, \tag{5}$$

Table 2 Exergy and energy balances and other expressions for system components

Component	Energy balance	Exergy balance
Expansion valve 1	$h_7 = h_8$	$\dot{\mathrm{E}}\mathrm{x}_7 = \dot{\mathrm{E}}\mathrm{x}_8 + \dot{\mathrm{E}}\mathrm{x}_{d_{\mathrm{EV1}}}$
Separator	$\dot{m}^8 = \dot{m}^9 + \dot{m}^{11}$ $\dot{m}_8 h_8 = \dot{m}_9 h_9 + \dot{m}_{11} h_{11}$	$\dot{\mathrm{E}}\mathrm{x}_8 = \dot{\mathrm{E}}\mathrm{x}_9 + \dot{\mathrm{E}}\mathrm{x}_{11} + \dot{\mathrm{E}}\mathrm{x}_{d_{\mathrm{Sep}}}$
Condenser 1	$\dot{m}_5 h_5 + \dot{m}_1 h_1 = \dot{m}_2 h_2 + \dot{m}_6 h_6$	$\dot{\mathrm{E}}\mathrm{x}_1 + \dot{\mathrm{E}}\mathrm{x}_5 = \dot{\mathrm{E}}\mathrm{x}_6 + \dot{\mathrm{E}}\mathrm{x}_2 + \dot{\mathrm{E}}\mathrm{x}_{d_{\mathrm{Cond.1}}}$
Turbine 2	$\dot{m}_4 h_4 = \dot{m}_1 h_1 + \dot{W}_{\mathrm{tur2}}$	$\dot{\mathrm{E}}\mathrm{x}_{d_{\mathrm{tur2}}} = (\dot{\mathrm{E}}\mathrm{x}_4 - \dot{\mathrm{E}}\mathrm{x}_1) + \dot{W}_{\mathrm{tur2}}$
Heat exchanger 1	$\dot{m}_3 h_3 + \dot{m}_9 h_9 = \dot{m}_4 h_4 + \dot{m}_{10} h_{10}$	$\dot{\mathrm{E}}\mathrm{x}_3 + \dot{\mathrm{E}}\mathrm{x}_9 = \dot{\mathrm{E}}\mathrm{x}_4 + \dot{\mathrm{E}}\mathrm{x}_{10} + \dot{\mathrm{E}}\mathrm{x}_{d_{\mathrm{HEX1}}}$
Pump 1	$\dot{m}_2 h_2 + \dot{W}_{p1} = \dot{m}_3 h_3$	$\dot{\mathrm{E}}\mathrm{x}_{d_{p1}} = (\dot{E}x_3 - \dot{E}x_2) + \dot{W}_{P1}$
Turbine 1	$\dot{m}_{11} h_{11} = \dot{m}_{12} h_{12} + \dot{W}_{\mathrm{tur1}}$	$\dot{\mathrm{E}}\mathrm{x}_{d_{\mathrm{tur1}}} = (\dot{\mathrm{E}}\mathrm{x}_{11} - \dot{\mathrm{E}}\mathrm{x}_{12}) + \dot{W}_{\mathrm{tur1}}$
LPG	$\dot{m}_{12} h_{12} + \dot{m}_{25} h_{25} = \dot{m}_{20} h_{20} + \dot{m}_{13} h_{13}$	$\dot{\mathrm{E}}\mathrm{x}_{12} + \dot{\mathrm{E}}\mathrm{x}_{25} = \dot{\mathrm{E}}\mathrm{x}_{20} + \dot{\mathrm{E}}\mathrm{x}_{13} + \dot{\mathrm{E}}\mathrm{x}_{d_{\mathrm{LPG}}}$
HEX 2	$\dot{m}_{20} h_{20} + \dot{m}_{24} h_{24} = \dot{m}_{25} h_{25} + \dot{m}_{21} h_{21}$ $\varepsilon_{\mathrm{HEX}} = (T_{20} - T_{21})/(T_{20} - T_{24})$	$\dot{\mathrm{E}}\mathrm{x}_{20} + \dot{\mathrm{E}}\mathrm{x}_{24} = \dot{\mathrm{E}}\mathrm{x}_{21} + \dot{\mathrm{E}}\mathrm{x}_{25} + \dot{\mathrm{E}}\mathrm{x}_{d_{\mathrm{HEX2}}}$
Pump 2	$\dot{m}_3 h_3 + \dot{W}_{p2} = \dot{m}_{24} h_{24}$	$\dot{\mathrm{E}}\mathrm{x}_d p_2 = (\dot{\mathrm{E}}\mathrm{x}_{23} - \dot{\mathrm{E}}\mathrm{x}_{24}) + \dot{W}_{P2}$
LPA	$\dot{m}_{27} h_{27} + \dot{m}_{22} h_{22} + \dot{m}_{38} h_{38} = \dot{m}_{28} h_{28} + \dot{m}_{23} h_{23}$	$\dot{\mathrm{E}}\mathrm{x}_{22} + \dot{\mathrm{E}}\mathrm{x}_{27} + \dot{\mathrm{E}}\mathrm{x}_{38} = \dot{\mathrm{E}}\mathrm{x}_{28} + \dot{\mathrm{E}}\mathrm{x}_{23} + \dot{\mathrm{E}}\mathrm{x}_{d_{\mathrm{LPA}}}$
Expansion valve 2	$h_{22} = h_{21}$	$\dot{\mathrm{E}}\mathrm{x}_{21} = \dot{\mathrm{E}}\mathrm{x}_{22} + \dot{\mathrm{E}}\mathrm{x}_{d_{\mathrm{EV2}}}$
Expansion valve 3	$h_{36} = h_{37}$	$\dot{\mathrm{E}}\mathrm{x}_{36} = \dot{\mathrm{E}}\mathrm{x}_{37} + \dot{\mathrm{E}}\mathrm{x}_{d_{\mathrm{EV3}}}$
Condenser 2	$\dot{m}_{35} h_{35} + \dot{m}_{39} h_{39} = \dot{m}_{40} h_{40} + \dot{m}_{36} h_{36}$	$\dot{\mathrm{E}}\mathrm{x}_{35} + \dot{\mathrm{E}}\mathrm{x}_{39} = \dot{\mathrm{E}}\mathrm{x}_{40} + \dot{\mathrm{E}}\mathrm{x}_{36} + \dot{\mathrm{E}}\mathrm{x}_{d_{Cond.2}}$
HPG	$\dot{m}_{34} h_{34} + \dot{m}_{10} h_{10} = \dot{m}_{35} h_{35} + \dot{m}_{29} h_{29} + \dot{m}_{14} h_{14}$	$\dot{\mathrm{E}}\mathrm{x}_{10} + \dot{\mathrm{E}}\mathrm{x}_{34} = \dot{\mathrm{E}}\mathrm{x}_{14} + \dot{\mathrm{E}}\mathrm{x}_{29} + \dot{\mathrm{E}}\mathrm{x}_{35} + \dot{\mathrm{E}}\mathrm{x}_{d_{\mathrm{HPG}}}$
Expansion valve 4	$h_{34} = h_{33}$	$\dot{\mathrm{E}}\mathrm{x}_{33} = \dot{\mathrm{E}}\mathrm{x}_{34} + \dot{\mathrm{E}}\mathrm{x}_{d_{\mathrm{EV4}}}$
Pump 3	$\dot{m}_{29} h_{29} + \dot{W}_{p3} = \dot{m}_{30} h_{30}$	$\dot{\mathrm{E}}\mathrm{x}_d p_3 = (\dot{\mathrm{E}}\mathrm{x}_{29} - \dot{\mathrm{E}}\mathrm{x}_{30}) + \dot{W}_{P3}$
Heat exchanger 3	$\dot{m}_{30} h_{30} + \dot{m}_{32} h_{32} = \dot{m}_{31} h_{31} + \dot{m}_{33} h_{33}$ $\varepsilon_{\mathrm{HEX}} = (T_{32} - T_{33})/(T_{32} - T_{30})$	$\dot{\mathrm{E}}\mathrm{x}_{32} + \dot{\mathrm{E}}\mathrm{x}_{30} = \dot{\mathrm{E}}\mathrm{x}_{31} + \dot{\mathrm{E}}\mathrm{x}_{33} + \dot{\mathrm{E}}\mathrm{x}_{d_{\mathrm{HEX3}}}$
HPA	$\dot{m}_{26} h_{26} + \dot{m}_{31} h_{31} + \dot{m}_{41} h_{41} = \dot{m}_{42} h_{42} + \dot{m}_{42} h_{42}$	$\dot{\mathrm{E}}\mathrm{x}_{31} + \dot{\mathrm{E}}\mathrm{x}_{26} + \dot{\mathrm{E}}\mathrm{x}_{41} = \dot{\mathrm{E}}\mathrm{x}_{42} + \dot{\mathrm{E}}\mathrm{x}_{32} + \dot{\mathrm{E}}\mathrm{x}_{d_{\mathrm{HPA}}}$
Expansion valve 5	$h_{14} = h_{15}$	$\dot{\mathrm{E}}\mathrm{x}_{14} = \dot{\mathrm{E}}\mathrm{x}_{15} + \dot{\mathrm{E}}\mathrm{x}_{d_{\mathrm{EV5}}}$
Mixer 1	$\dot{m}_{13} h_{13} + \dot{m}_{15} h_{15} = \dot{m}_{17} h_{17} + \dot{m}_{16} h_{16}$	$\dot{\mathrm{E}}\mathrm{x}_{13} + \dot{\mathrm{E}}\mathrm{x}_{15} = \dot{\mathrm{E}}\mathrm{x}_{116} + \dot{\mathrm{E}}\mathrm{x}_{17} + \dot{\mathrm{E}}\mathrm{x}_{d_{\mathrm{Mixer1}}}$
Mixer 2	$\dot{m}_{18} h_{18} + \dot{m}_{17} h_{17} = \dot{m}_{19} h_{19}$	$\dot{\mathrm{E}}\mathrm{x}_{17} + \dot{\mathrm{E}}\mathrm{x}_{18} = \dot{\mathrm{E}}\mathrm{x}_{19} + \dot{\mathrm{E}}\mathrm{x}_{d_{\mathrm{Mixer2}}}$
Heat exchanger 4	$\dot{m}_{16} h_{16} + \dot{m}_{45} h_{45} = \dot{m}_{18} h_{18} + \dot{m}_{46} h_{46}$	$\dot{\mathrm{E}}\mathrm{x}_{16} + \dot{\mathrm{E}}\mathrm{x}_{45} = \dot{\mathrm{E}}\mathrm{x}_{18} + \dot{\mathrm{E}}\mathrm{x}_{46} + \dot{\mathrm{E}}\mathrm{x}_{d_{\mathrm{HEX4}}}$
PEME	See PEME modeling	$\dot{\mathrm{E}}\mathrm{x}_{46} = \dot{\mathrm{E}}\mathrm{x}_{\mathrm{H}_2} + \dot{\mathrm{E}}\mathrm{x}_{\mathrm{O}_2} + \dot{\mathrm{E}}\mathrm{x}_{d_{\mathrm{PEME}}}$

where LHV_{H_2} is the lower heating value of H_2 and the total harvested geothermal energy is:

$$\dot{Q}_{geo} = \dot{m}_7(h_7 - h_{19}).$$

Proton exchange membrane electrolyzer

The electrical power generated in turbine 1 (Tur. 1) drives the electrolyzer. The electrolyzer's anode side reaction consists of the oxidative process of water, resulting in the generation of oxygen gas, protons (H^+), and electrons (e^-). It can be represented as (Safari and Dincer 2018):

$$H_2O \rightarrow 2H^+ + 0.5O_2 + 2e^{-1} \tag{6}$$

The cathode side reaction in the electrolyzer involves reducing protons (H^+) and electrons (e^-) to produce hydrogen gas. It can be represented as (Safari and Dincer 2018):

$$2H^+ + 2e^{-1} \rightarrow H_2 \tag{7}$$

The overall reaction in the electrolyzer combines the cathode and anode side reactions. It can be represented as (Safari and Dincer 2018):

$$2H_2O \rightarrow 2H_2 + O_2 \tag{8}$$

In this general reaction, water molecules are divided into oxygen gas (O_2) at the anode and hydrogen gas (H_2) at the cathode.

The following relation describes the hydrogen production rate (Nami et al. 2018, 2017):

$$\dot{m}_{H_2} = \frac{J}{2F}. \tag{9}$$

Here, $\dot{m}_{H_2}$ denotes hydrogen production rate, F the Faraday constant, and J current density.

The power needed to operate the electrolyzer, denoted as $\dot{W}_{PEME}$, can be written as (Cao et al. 2020):

$$\dot{W}_{PEME} = \dot{W}_{tur1} = J \times V. \tag{10}$$

Here, $\dot{W}_{tur2}$ denotes the generated power in turbine 1, and V is the voltage applied to the electrolyzer. In this case, V represents the voltage across the electrolyzer, which can be expressed as the sum of several components (Cao et al. 2020):

$$V = V_0 + V_{act,a} + V_{act,c} + V_{ohm}, \tag{11}$$

where V_0 is the reversible potential, which is the thermodynamically balanced voltage where no net current flows during a redox reaction, while $V_{act,a}$, the anode-side activation potential, is the additional potential required at the anode to initiate or facilitate the electrochemical reaction. $V_{act,c}$ is the cathode-side activation potential, which represents the extra potential necessary at the cathode for the electrochemical reaction to occur. V_{ohm} is the ohmic potential that arises due to the resistance encountered by the current flow within the electrolyte or other conductive materials.

The reversible potential can be written by employing the subsequent relation (Safari and Dincer 2018):

$$V_0 = 1.229 - 8.5 \times 10^{-4}(T_{\mathrm{PEME}} - 298\mathrm{K}). \tag{12}$$

This allows the potential of activation of the cathode and anode sides of the power supply to be determined.

The activation potential ($V_{\mathrm{act},i}$) for either the anode ($i=a$) or cathode ($i=c$) side of the power supply is expressible as (Cao et al. 2020):

$$V_{\mathrm{act},i} = \frac{(R \times T_{\mathrm{PEME}})}{F} \times \sinh^{-1}\left(\frac{J}{2 \times J_{0,i}}\right), i = a, c, \tag{13}$$

where R is the characteristic gas constant of hydrogen.

The term $J_{0,i}$ represents the exchange current density at either the cathode ($i=c$) or anode ($i=a$) side of the power supply. It can be expressed as:

$$J_{0,i} = J_{\mathrm{ref},i} \times \exp\left(-\frac{E_{\mathrm{act},i}}{RT_{\mathrm{PEME}}}\right), i = a, c, \tag{14}$$

where $E_{\mathrm{act},i}$ is the energy of activation for the electrochemical reaction at the respective electrode side and $J_{\mathrm{ref},i}$ is the reference exchange current density.

The ohmic potential (V_{ohm}) can be written as:

$$V_{\mathrm{ohm}} = J \times R_{\mathrm{PEME}}. \tag{15}$$

Here, J denotes the current density, and R_{PEME} is the resistance of the polymer electrolyte membrane, which can be expressed as

$$R_{\mathrm{PEME}} = \int_0^L \frac{\mathrm{d}x}{\sigma_{\mathrm{PEME}}(\lambda(x))}. \tag{16}$$

Here, $\sigma_{\mathrm{PEME}}(\lambda(x))$ is the local ionic conductivity coefficient, while $\lambda(x)$ is the water content in the polymer electrolyte membrane, determined as:

$$\sigma_{\mathrm{PEME}}(\lambda(x)) = (0.5139\lambda(x) - 0.326)\left(1268\left(\frac{1}{303K} - \frac{1}{T_{\mathrm{PEME}}}\right)\right), \tag{17}$$

$$\lambda(x) = \frac{(\lambda_a - \lambda_c)}{D} \times x + \lambda_c. \tag{18}$$

Exergoeconomic analysis

A cost conservation equation for each component in the system can be formulated in the following manner (Aghaziarati and Aghdam 2021; Balaji 2021):

$$\dot{C}_q + \sum_k \dot{C}_{\mathrm{in},k} + \dot{Z}_k = \dot{C}_w + \sum_k \dot{C}_{\mathrm{out},k}. \tag{19}$$

Here, $\dot{C}_{\mathrm{out},k}$ denotes the cost rate of the output flow for each component, $\dot{C}_{\mathrm{in},k}$ is the cost rate of the input flow for each component, and $\dot{C}_w$ denotes the cost rate of the work. The

relationship between the unit cost, exergy rate, and cost rate follows (Gholizadeh et al. 2020):

$$\dot{C}_k = c_k \dot{\mathrm{E}}\mathrm{x}_k. \tag{20}$$

The expression below denotes the relative cost difference, r_k, showing the relative rise in the average cost per exergy unit between fuel and product of the element, which is calculated for each element as follows (Nikam et al. 2021):

$$r_k = \frac{c_{P,k} - c_{F,k}}{c_{F,k}}. \tag{21}$$

The cost rate for all components can be expressed as follows:

$$\dot{Z}_k = \mathrm{CRF} \times \left(\frac{\varphi_r \times 365 \times 24}{N} \right) \times Z_k. \tag{22}$$

Here, Z_k is the capital cost of each element, N is the hours of operation per year, ϕ_r is the maintenance coefficient, and CRF denotes the capital recovery factor, which is expressible as:

$$\mathrm{CRF} = \frac{I_r(1+I_r)^\tau}{(1+I_r)^\tau - 1}, \tag{23}$$

where I_r is the initial capital investment, and τ is the number of years over which the investment will be recovered.

To calculate the surface area of heat exchangers employing the logarithmic mean temperature difference (LMTD), the following equation is utilized:

$$A_k = \frac{\dot{Q}_k}{U_k \times \Delta T_{\mathrm{LMTD}}}. \tag{24}$$

The following equation is utilized to compute the logarithmic mean temperature difference:

$$\mathrm{LMTD} = \frac{(\Delta T_1 - \Delta T_2)}{ln\left(\frac{\Delta T_1}{\Delta T_2}\right)}, \tag{25}$$

where ΔT_1 and ΔT_2 are the temperature difference between the cold and hot flows at the inlet and outlet of the heat exchanger, respectively.

The overall heat transfer coefficients of different heat components are 2.5 kW/m^2 K for the condenser, 1.5 kW/m^2 K for the evaporator, 1.5 kW/m^2 K for the vapor generator, and 1.1 kW/m^2 K for the heat exchanger. The heat transfer coefficient for absorbers is 2 kW/m^2 K (Fu et al. 2022; Maryami and Dehghan 2017; Mohammadkhani et al. 2014). Table 3 provides the auxiliary equations, cost function, and cost conservation expressions. The unit polygeneration cost, UPGC, can be expressed in terms of unit cost:

$$\mathrm{UPGC} = \frac{\dot{C}_{44} + \dot{C}_{\dot{W}} + \dot{C}_{H_2}}{\dot{W}_{\mathrm{tur2}} + \dot{\mathrm{E}}\mathrm{x}_{P_{\mathrm{ev}}} + \dot{\mathrm{E}}\mathrm{x}_{P_{\mathrm{PEME}}}}. \tag{26}$$

The combined exergy and economic formulations are given in Table 4.

The exergy efficiency of the proposed system is:

$$\eta_e = \frac{\dot{W}_{t\mathrm{ur2}} + \dot{\mathrm{E}}\mathrm{x}_{P_{\mathrm{ev}}} + \dot{\mathrm{E}}\mathrm{x}_{P_{\mathrm{PEME}}}}{\dot{\mathrm{E}}\mathrm{x}_5 - \dot{\mathrm{E}}\mathrm{x}_{47}}. \tag{27}$$

The equations are solved using Engineering Equation Solver (EES). Properties such as enthalpy and entropy of flows at various locations are calculated utilizing the internal libraries of this software.

For instance, the properties of the lithium bromide–water solution are calculated using the $\mathrm{LiBrH_2O}$ library in EES.

Validation

To evaluate the efficiency of the proposed system, it is necessary to confirm and validate its performance using independent sources, such as existing research conducted in this particular domain. This section begins with a validation process and then investigates the various design parameters. To validate the current study for simulating the half-effect absorption chiller, the study of Maryami and Dehghan (2017) is used. The results are presented in Table 5. A slight discrepancy between the calculated values can be observed. The COP obtained in the current study is 0.435, whereas the reference value is 0.438 (i.e., different by less than 1%). These values are similar, indicating that the differences in the data points have only a minor effect on the final results and are insignificant.

To further validate our simulation of absorption chillers, we conducted another verification test by comparing our study's results with the theoretical and experimental investigation conducted by Florides et al. (2003). Their study involved the design and construction of a single-effect LiBr/water absorption chiller with a capacity of 10 kW. The constraints and comparisons of the outputs between their study and the current investigation are detailed in Table 6. The inputs and comparisons of our study with the investigation of Florides et al. (2003) are provided in Tables 6 and 7, respectively. All differences are observed to be less than 4%. These slight disparities may be attributed to the accuracy of the correlations used to predict the properties of the LiBr/water solution in EES. However, these differences are not significant and fall within acceptable ranges.

The current study on geothermal and organic Rankine cycle simulation is validated using the research conducted by Shokati and Ranjbar (2015). A comparison between the

Table 3 Balance of cost for multigeneration plant components

Component	Cost balance	Auxiliary equation	Capital cost	Refs.
HEX 1	$\dot{C}_9 + \dot{C}_3 + \dot{Z}_{HEX1} = \dot{C}_4 + \dot{C}_{10}$		$Z_{HEX1} = 130\left(\frac{A_{HEX1}}{0.093}\right)^{0.78}$	Mohammadkhani et al. (2014)
Expansion valve 1	$\dot{C}_7 + \dot{Z}_{EV1} = \dot{C}_8$	$c_7 = c_8$		
Separator	$\dot{C}_8 = \dot{C}_9 + \dot{C}_{10}$	$c_8 = c_9 = c_{10}$		
Turbine 2	$\dot{C}_4 + \dot{Z}_{tur2} = \dot{C}_1 + \dot{C}w_{tur2}$	$c_1 = c_4$	$Z_{tur2} = 1356 \times \dot{m}_1/(0.92 - \eta_{tur}) \times (P_1/P_4) \times (1 + \exp(0.036 \times T_4 - 54.4))$	Mohammadkhani et al. (2014)
Pump 1	$\dot{C}_2 + \dot{Z}_{p1} + \dot{C}_{w,p1} = \dot{C}_3$	$c_1 = c_2$ $\frac{\dot{C}_{wtur2}}{\dot{W}_{tur2}} = \frac{\dot{C}_{wp1}}{\dot{W}_{p1}}$	$Z_{p1} = 3540 \times \left(\dot{W}_{p1}\right)^{0.71}$	Mohammadkhani et al. (2014)
Condenser 1	$\dot{C}_1 + \dot{C}_5 + \dot{Z}_{Cond.1} = \dot{C}_2 + \dot{C}_6$		$Z_{Cond.1} = 1777\dot{m}_1$	Mohammadkhani et al. (2014)
Turbine 1	$\dot{C}_{11} + \dot{Z}_{T1} = \dot{C}_{12} + \dot{C}w_{tur1}$		$Z_{tur1} = 1356 \times \dot{m}_{12}/(0.92 - \eta_{tur}) \times \left(\frac{P_{12}}{P_{11}}\right) \times (1 + \exp(0.036 \times T_{11} - 54.4))$	Mohammadkhani et al. (2014)
HPG	$\dot{C}_{10} + \dot{C}_{34} + \dot{Z}_{HPG} = \dot{C}_{29} + \dot{C}_{35} + \dot{C}_{14}$	$c_{14} = c_{10}$ $\frac{\dot{C}_{35}+\dot{C}_{29}}{\dot{E}x_{35}+\dot{E}x_{29}} = \frac{\dot{C}_{34}}{\dot{E}x_{34}}$	$Z_{HPG} = 1800 \times (10.76 \times A_{HPG})^{0.8} + 24915$	Fu et al. (2022)
Condenser	$\dot{C}_{35} + \dot{C}_{39} + \dot{Z}_{Cond.2} = \dot{C}_{40} + \dot{C}_{36}$	$c_{35} = c_{36}$ $c_{39} = 0$	$Z_{Cond.2} = 2119 \times (10.76A_{Cond.2})^{0.497}$	Fu et al. (2022)
Expansion valve 3	$\dot{C}_{36} = \dot{C}_{37}$			
Evaporator	$\dot{C}_{37} + \dot{C}_{43} + \dot{Z}_{ev} = \dot{C}_{44} + \dot{C}_{38}$	$c_{43} = 0$ $c_{37} = c_{38}$	$Z_{ev} = 5900 \times (10.76 \times A_{ev})^{0.552}$	Fu et al. (2022)
LPG	$\dot{C}_{25} + \dot{C}_{12} + \dot{Z}_{LPA} = \dot{C}_{20} + \dot{C}_{13}$	$\frac{\dot{C}_{26}+\dot{C}_{20}}{\dot{E}x_{26}+\dot{E}x_{20}} = \frac{\dot{C}_{25}}{\dot{E}x_{25}}$ $c_{12} = c_{13}$	$9.976 \times (10.76 \times A_{LPG})^{1.820}$	Fu et al. (2022)
Pump 2	$\dot{C}_{23} + \dot{Z}_{p2} + \dot{C}_{wp2} = \dot{C}_{24}$	$c_{23} = c_{24}$ $\frac{\dot{C}_{Wtur1}}{\dot{W}_{tur1}} = \frac{\dot{C}_{Wp2}}{\dot{W}_{p2}}$	$Z_{p2} = 3540 \times \left(W_{p2}\right)^{0.71}$	Mohammadkhani et al. (2014)
Expansion valve 3	$\dot{C}_{21} = \dot{C}_{22}$			

Table 3 (continued)

Component	Cost balance	Auxiliary equation	Capital cost	Refs.
HEX 2	$\dot{C}_{20}+\dot{C}_{24}+\dot{Z}_{\mathrm{HEX2}}=\dot{C}_{25}+\dot{C}_{21}$	$c_{20}=c_{21}$	$Z_{\mathrm{HEX2}}=2674\times(10.76\times A_{\mathrm{HEX2}})^{0.465}$	Fu et al. (2022)
HPA	$\dot{C}_{26}+\dot{C}_{31}+\dot{C}_{41}+\dot{Z}_{\mathrm{HPA}}=\dot{C}_{32}+\dot{C}_{42}$	$c_{41}=0$ $\frac{\dot{C}_{26}+\dot{C}_{31}}{\dot{E}x_{26}+\dot{E}x_{31}}=\frac{\dot{C}_{32}}{\dot{E}x_{32}}$	$9.976\times(10.76\times A_{\mathrm{HPA}})^{1.820}$	Fu et al. (2022)
HEX 3	$\dot{C}_{30}+\dot{C}_{32}+\dot{Z}_{\mathrm{HEX3}}=\dot{C}_{31}+\dot{C}_{33}$	$c_{30}=c_{31}$	$Z_{\mathrm{HEX3}}=2674\times(10.76\times A_{\mathrm{HEX3}})^{0.465}$	Fu et al. (2022)
Expansion valve 4	$\dot{C}_{33}=\dot{C}_{34}$			
Pump 3	$\dot{C}_{29}+\dot{Z}_{p3}+\dot{C}_{wp3}=\dot{C}_{30}$		$Z_{p3}=3540\times\left(\dot{W}_{p3}\right)^{0.71}$	Mohammadkhani et al. (2014)
LPA	$\dot{C}_{38}+\dot{C}_{27}+\dot{C}_{22}+\dot{Z}_{\mathrm{LPA}}=\dot{C}_{23}+\dot{C}_{28}$	$c_{27}=0$ $\frac{\dot{C}_{22}+\dot{C}_{38}}{\dot{E}x_{22}+\dot{E}x_{38}}=\frac{\dot{C}_{23}}{\dot{E}x_{23}}$	$9.976\times(10.76\times A_{\mathrm{LPA}})^{1.820}$	
Expansion valve 5	$\dot{C}_{14}=\dot{C}_{15}$			
Mixer 1	$\dot{C}_{13}+\dot{C}_{15}=\dot{C}_{17}+\dot{C}_{16}$			
Mixer 2	$\dot{C}_{17}+\dot{C}_{18}=\dot{C}_{19}$			
HEX 4	$\dot{C}_{16}+\dot{C}_{45}+\dot{Z}_{\mathrm{HEX4}}=\dot{C}_{18}+\dot{C}_{46}$	$c_{16}=c_{18}$ $c_{45}=0$	$2674\times(10.76\times A_{\mathrm{HEX4}})^{0.465}$	Fu et al. (2022)
PEME	$\dot{C}_{46}+\dot{C}_{W,\mathrm{tur1}}+\dot{Z}_{\mathrm{PEME}}=\dot{C}_{H_2}+\dot{C}_{O_2}$	$c_{O_2}=c_{H_2}$	$Z_{\mathrm{PEME}}=24\times4\times\dot{m}_{46}$	Azariyan et al. (2021)

Table 4 Extra cost and exergy equations of the multigeneration plant components

Component	$\dot{E}x_F$	$\dot{E}x_P$	r_k
Turbine 2	$\dot{E}x_4 - \dot{E}x_1$	$\dot{W}_{tur2}$	$\frac{\left(\frac{\dot{C}_{Wtur2}}{\dot{W}_{tur2}} - c_4\right)}{c_4}$
Condenser 1	$\dot{E}x_1 - \dot{E}x_2$	$\dot{E}x_6 - \dot{E}x_5$	$\frac{c_6 - c_1}{c_1}$
Pump 1	$\dot{W}_{p1}$	$\dot{E}x_3 - \dot{E}x_2$	$\frac{c_3 - \frac{\dot{C}_{Wp1}}{\dot{W}_{p1}}}{\frac{\dot{C}_{Wp1}}{\dot{W}_{p1}}}$
HEX 1	$\dot{E}x_9 - \dot{E}x_{10}$	$\dot{E}x_4 - \dot{E}x_3$	$\frac{c_4 - c_9}{c_9}$
Turbine 1	$\dot{E}x_{11} - \dot{E}x_{12}$	$\dot{W}_{tur1}$	
Condenser 2	$\dot{E}x_{35} - \dot{E}x_{36}$	$\dot{E}x_{40} - \dot{E}x_{39}$	$\frac{c_{40} - c_{35}}{c_{35}}$
Evaporator	$\dot{E}x_{37} - \dot{E}x_{38}$	$\dot{E}x_{44} - \dot{E}x_{43}$	$\frac{c_{44} - c_{37}}{c_{37}}$
LPH	$\dot{E}x_{23} - \dot{E}x_{22} + \dot{E}x_{38}$	$\dot{E}x_{28} - \dot{E}x_{27}$	$\frac{(c_{28} - c_{23})}{c_{23}}$
HEX 2	$\dot{E}x_{20} - \dot{E}x_{21}$	$\dot{E}x_{25} - \dot{E}x_4$	$\frac{c_{25} - c_{20}}{c_{20}}$
Pump 2	$\dot{W}_{p2}$	$\dot{E}x_{24} - \dot{E}x_{23}$	
LPG	$\dot{E}x_{12} - \dot{E}x_{13}$	$\dot{E}x_{20} + \dot{E}x_{26} - \dot{E}x_{25}$	$\frac{c_{20} - c_{12}}{c_{12}}$
HPA	$\dot{E}x_{32} - \dot{E}x_{26} - \dot{E}x_{31}$	$\dot{E}x_{42} - \dot{E}x_{41}$	$\frac{c_{42} - c_{32}}{c_{32}}$
Pump 3	$\dot{W}_{p3}$	$\dot{E}x_{30} - \dot{E}x_{29}$	$\frac{c_{30} - \frac{\dot{C}_{Wp3}}{\dot{W}_{p3}}}{\frac{\dot{C}_{Wp3}}{\dot{W}_{p3}}}$
HEX 3	$\dot{E}x_{32} - \dot{E}x_{33}$	$\dot{E}x_{31} - \dot{E}x_{30}$	$\frac{(c_{31} - c_{32})}{c_{32}}$
HPG	$\dot{E}x_{10} - \dot{E}x_{14}$	$\dot{E}x_{29} + \dot{E}x_{35} - \dot{E}x_{34}$	$\frac{c_{29} - c_{10}}{c_{10}}$
PEME	$\dot{W}_{tur1}$	$\dot{E}x_{H_2} + \dot{E}x_{O_2} - \dot{E}x_{46}$	$\frac{c_{H_2} - \frac{\dot{C}_{Wtur1}}{\dot{W}_{tur1}}}{\frac{\dot{C}_{Wtur1}}{\dot{W}_{tur1}}}$

Table 5 Comparison of the current study and the study of Maryami and Dehghan (2017)

	T (°C)		P (kPa)		x (%)		$\dot{m}$ (kg/s)		h (kJ/kg)		s (kJ/kg K)	
Point	CS[a]	Ref.a	CS	Ref	CS	Ref	CS	Ref	CS	Ref	CS	Ref
1	33	33	1.23	1.23	51.41	51.4	0.94	0.94	69.13	69.1	0.22	0.22
2	33	33	2.26	2.26	51.41	51.4	0.94	0.94	69.13	69.1	0.22	0.22
3	48	47	2.26	2.26	51.41	51.4	0.94	0.94	69.13	99.1	0.32	0.33
4	58	58	2.26	2.26	59.41	59.1	0.81	0.81	101.40	146.6	0.32	0.33
5	39	41	2.26	2.26	59.41	59.1	0.81	0.81	148.00	112.1	0.22	0.22
6	39	47	1.23	1.23	59.41	59.1	0.81	0.81	110.80	112.1	0.26	0.22
7	33	33	2.26	2.26	44.40	43.1	0.83	0.83	110.80	64.0	0.29	0.28
8	33	33	5.04	5.03	44.40	43.1	0.83	0.83	63.68	64.1	0.29	0.28
9	48	47	5.04	5.03	44.40	43.1	0.83	0.83	63.68	96.3	0.39	0.39
10	58	58	5.04	5.03	52.40	51.1	0.70	0.70	98.34	123.1	0.39	0.38
11	39	41	5.04	5.03	52.40	51.1	0.70	0.70	125.10	84.9	0.28	0.26
12	39	43	2.26	2.26	52.40	51.1	0.70	0.70	84.23	84.9	0.29	0.26
13	58	48	5.04	5.03			0.13	0.13	84.23	84.2	8.54	8.48
14	33	33	5.04	5.03			0.13	0.13	2578.90	2609.0	0.48	0.48
15	10	10	1.23	1.23			0.13	0.13	138.20	138.3	0.49	0.49
16	10	10	1.23	1.23			0.13	0.13	138.20	138.3	8.90	8.90
17	58	44	2.26	2.26			0.13	0.13	2581.40	2519.0	8.83	8.83

[a] CS denotes the current study, and Ref. is the study of Maryami and Dehghan (2017)

Table 6 Inputs for validation of the current study and the investigation of Florides et al. (2003)

Parameter	Value
Solution temperature at the desorber outlet (C)	90
Water vapor temperature at the desorber oulet (C)	85
Condenser pressure (kPa)	9.66
Evaporator temperature (C)	6
Solution temperature at the absorber outlet (C)	34.9
Evaporator heat load (kW)	10
Solution heat exchanger efficiency	0.522

Table 7 Comparison of the results of the current study and the investigation of Florides et al. (2003)

Parameter	Current study	Florides et al. (2003)	Difference (%)[a]
$\dot{Q}_{gen}$	14.55	14.2	2.5
$\dot{Q}_{con}$	10.63	10.78	1.4
$\dot{Q}_{abs}$	13.92	13.51	3.0
$\dot{W}_{pump}$	0.278	0.29	4.1
COP	0.687	0.704	2.4

[a] This is the magnitude of difference on a percentage basis, calculated considering the study of Florides et al. (2003) as the basis

two studies is presented in Table 8, showing that the results are almost identical, and the differences are minor, as seen in the last column of the table.

These findings indicate that the current study is reliable and accurate and that the geothermal and organic Rankine cycle simulations have been executed reasonably accurately.

In order to validate the accuracy of the electrolysis simulation in this investigation, the experimental research conducted by Ioroi et al. (2002) is utilized. The validation of the electrolyzer is presented in Fig. 2, which clearly demonstrates that the voltage gained from the present work is in close agreement (less than 5% discrepancy in the worst case) with the outcomes obtained in the research of Ioroi et al. (2002). Therefore, it can be concluded that the current study is sufficiently accurate in its simulation of electrolysis.

Results and discussion

This section provides a detailed examination of the system, beginning with an assessment of its current status, followed by a comprehensive study. The results of thermodynamic and exergoeconomic evaluations are obtained using the data listed in Table 1. These results are presented in Table 9. According to the findings presented, multigeneration has thermal and exergy efficiencies of 19.6% and 26.6%, respectively, and a unit cost of 9.02 $/GJ. According to the energy efficiency definition (Eq. 5 of the current paper), the cooling rate product ($Q_{eva} = 329$ kW) significantly influences energy efficiency more than power ($\dot{W}_{net} = 152$ kW) and hydrogen production rate ($\dot{m}_{H2} = 1.10$ kg/h). Considering the total harvested geothermal energy, $Q_{geo} = 2704$ kW, it can be seen that about 6% is converted to electrical power, about 12% is converted to cooling, and about 1% is the share of hydrogen production. Note that the unit cost associated with cooling (106

Table 8 Comparison of the current study and the study of Shokati and Ranjbar (2015)

Point	*T* (°C)		P (kPa)		$\dot{m}$ (kg/s)		$\dot{E}x$ (kW)		Difference in $\dot{E}x$ (%)[b]
	CS[a]	Ref.[a]	CS	Ref	CS	Ref	CS	Ref	
1	78.19	78.2	154.7	154.7	109.7	109.7	1270	1261	0.71
2	40	40	154.7	154.7	109.7	109.7	50.68	51.98	2.50
3	40.32	40.32	786.8	786.8	109.7	109.7	99.88	101.2	1.30
4	119.6	119.6	786.8	786.8	109.7	109.7	4477	4468	0.20
5	162	162			100	100	10,367	10,367	0.00
6	129.6	129.6	266.7	266.7	100	100	9941	9941	0.00
7	129.6	129.6	266.7	266.7	6.422	6.427	4037	4036	0.02
8	129.6	129.6	266.7	266.7	93.58	93.57	5904	5905	0.01
9	69.09	69.09	30	30	6.422	6.427	1866	1862	0.21
10	69.09	69.09	30	30	6.422	6.427	78.79	79.4	0.76
11	69.09	69.09	30	30	93.58	93.57	1148	1178	2.54

[a] CS denotes the current study, and Ref. is the Reference (Shokati and Ranjbar 2015)

[b] This is the magnitude of difference on a percentage basis, calculated considering the study of Shokati and Ranjbar (2015) as the basis

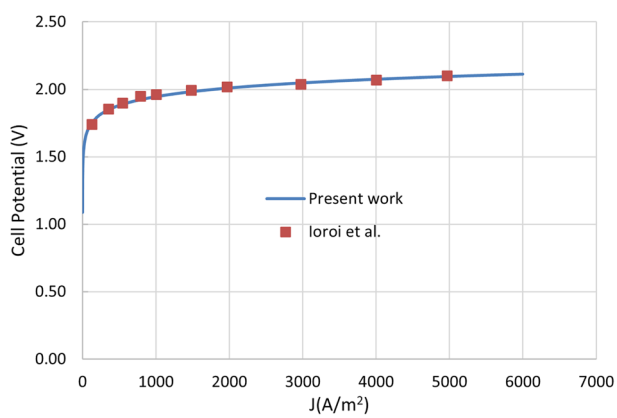

Fig. 2 Comparison of the current study and the study of Ioroi et al. (2002)

$/GJ) is higher than the unit costs for electrical power or hydrogen production, which means that cooling is more costly and requires a greater financial investment.

Table 10 summarizes the thermodynamic characteristics, unit costs, and cost flow rates associated with various system states under the base case working conditions.

Table 11 displays the economic and exergy parameters for each plant element. The results show that the highest exergy consumption occurs in the ORC and heat exchanger HEX 1, with a value of 454.4 kW. This is mainly because of the high temperature and pressure present in the element as well as the high-temperature difference with the source. Furthermore, the separators and mixers exhibit the lowest destruction rates of exergy compared to the other devices of the proposed system, which have not been reported. In addition, HEX 1 experiences the maximum exergy destruction rate among the plant elements, at 240.9 kW, due to becoming superheated after the phase change of the pure fluid in the ORC side and the high-temperature difference between the cold and hot flows. Furthermore, the maximum annual cost is associated with the high-pressure absorber component, HPA.

Table 9 Results of exergoeconomic and thermodynamic analyses

Parameter	Unit	Amount
Net output power	kW	151.8
Turbine 2 power	kW	164
Power of pump 1	kW	2.94
Power of pump 2	kW	6.90
Power of pump 3	kW	2.37
PEME power (Turbine 1)	kW	127
Condenser 1 duty ($\dot{Q}_{Cond1}$)	kW	351.4
Condenser 2 duty ($\dot{Q}_{Cond2}$)	kW	1062
LPG duty ($\dot{Q}_{LPG}$)	kW	959.8
HPG duty ($\dot{Q}_{HPG}$)	kW	403.4
LPA duty ($\dot{Q}_{LPA}$)	kW	463.2
HPA duty ($\dot{Q}_{HPA}$)	kW	886.6
Evaporator duty ($\dot{Q}_{ev}$)	kW	328.6
Total geothermal harvested heat rate	kW	2704
Hydrogen production rate ($\dot{m}_{H_2}$)	kg/h	1.097
Exergy efficiency (η_e)	%	26.63
Thermal efficiency (η_t)	%	19.57
Unit cost of cooling	$/GJ	106.1
Unit cost of producing power	$/GJ	1.62
Unit hydrogen production cost	$/GJ	5.73
UPGC	$/GJ	9.024

Table 11 also provides information on the relative cost difference for multiple system elements. The table shows that components like condensers (Condenser 1 and 2), pumps (Pump 2 and 3), and heat exchangers in the absorption side (LPA, HPG, HPA, LPG) have significantly high relative cost difference values. This is likely due to their high cost per unit exergy of the product, which is much greater than the cost per unit exergy of the fuel, owing to their high rates of destruction of exergy and low exergy efficiency, as determined in a previous study (Chakyrova 2019; Doseva and Chakyrova 2015). Diverse values have been reported for r in the literature, ranging from negative (Singh and Kaushik 2013) to greater than 100% in references (Balli and Caliskan 2022; Farshi et al. 2013; Toro and Sciubba 2018).

Exergy analysis provides a means to integrate sustainability considerations and assess the environmental influence of energy-consuming systems. A higher exergy efficiency often indicates greater sustainability, which in turn suggests a lower environmental impact, and vice versa. Therefore, exergy analysis is a helpful instrument in evaluating the performance of energy systems from a sustainability perspective (Aygun 2021). The exergy efficiencies of various system components are presented in Fig. 3. The maximum η_e is associated with the turbines and the lowest with the pumps. Devices with low exergy efficiencies, such as the mentioned pump, should be redesigned to improve the total efficiencies.

Table 10 Thermodynamic characteristics and costs of different states for the system under base case working conditions

No.	*P* (kPa)	$\dot{m}$ (kg/s)	*T* (°C)	*S* (kJ/kg-°C)	*H* (kJ/kg)	$\dot{E}x$ (kW)	$\dot{C}$ ($/h)	*c* ($/GJ)
1	109.7	5.362	66.15	1.751	427.6	26.8	0.21492	2.23
2	109.7	5.362	30	1.109	231.4	0.2673	0.002142	2.23
3	786.8	5.362	30.32	1.109	231.9	2.782	0.14292	14.3
4	786.8	5.362	117.4	1.735	458.2	216.3	1.7352	2.23
5	100	50.34	25	0.3672	104.8	0	0	0
6	100	50.34	30	0.4368	125.7	9.305	0.3708	11.1
7	266	10	150	1.842	632.2	879.3	4.2912	1.36
8	250	10	127.4	1.849	632.2	857.9	4.1868	1.36
9	250	9.556	127.4	1.607	535.3	582.9	2.844	1.36
10	250	9.556	97.41	1.278	408.4	307.7	0.6264	1.36
11	250	0.4439	127.4	7.053	2717	275	1.3428	1.36
12	30	0.4439	69.09	7.2	2430	128.5	0.6264	1.36
13	30	0.4439	64.09	0.8824	268.3	4.424	0.0216	1.36
14	250	9.556	87.41	1.163	366.2	231.7	1.1304	1.36
15	30	9.556	69.09	1.156	361.8	209.5	1.152	1.46
16	100	0.000533	69.09	1.156	361.8	0.01168	0.00006156	1.46
17	30	10	69.09	1.156	361.8	219.2	1.152	1.46
18	30	0.000533	64.09	0.8824	268.3	0.005309	0.0000279	1.46
19	30	10	69.09	1.156	361.8	219.2	1.152	1.46
20	3.251	3.624	64.09	0.36	165.5	3042	148.68	13.6
21	3.251	3.624	42.91	0.2377	125.1	3028	147.96	13.6
22	0.8725	3.624	42.91	0.2377	125.1	3028	147.96	13.6
23	0.8725	3.95	35	0.2091	85.88	2953	143.964	13.5
24	3.251	3.95	35.85	0.2147	87.63	2954	143.964	13.5
25	3.251	3.95	53.96	0.3298	124.7	2965	145.008	13.6
26	3.251	0.3254	64.09	8.778	2620	19.28	1.0728	15.4
27	100	22.16	25	0.3672	104.8	0	0	0
28	100	22.16	30	0.4368	125.7	4.096	3.618	245
29	5.629	0.9512	92.41	0.7755	213.6	493.3	18.702	10.5
30	5.629	0.9512	46.21	0.434	98.23	480.3	18.2124	10.5
31	3.251	0.9512	46.21	0.434	98.23	480.3	18.2124	10.5
32	3.251	1.09	30	0.3397	54.5	471.3	18.1908	10.7
33	5.629	1.09	30.81	0.3468	56.67	471.4	18.1908	10.7
34	5.629	1.09	68.03	0.6571	157.4	480.4	18.81	10.9
35	5.629	0.1391	92.41	8.676	2674	19.85	1.3932	19.5
36	5.629	0.1391	35	0.5051	146.6	7.061	0.4968	19.5
37	0.8725	0.1391	5	0.5279	146.6	6.119	0.4284	19.5
38	0.8725	0.1391	5	9.025	2510	− 17.34	− 1.224	19.5
39	100	16.88	25	0.3672	104.9	1.502	0	0
40	100	16.88	30	0.4368	125.7	3.12	1.2312	110
41	100	42.41	25	0.3672	104.8	0	0	0
42	100	42.41	30	0.4368	125.7	7.84	4.0824	145
43	100	5.232	25	0.3672	104.8	0	0	0
44	100	5.232	10	0.1511	42.02	8.38	2.8584	94.8
45	100	0.000305	25	0.3672	104.8	0	0	0
46	100	0.000305	64.09	0.8824	268.3	0.01825	0.006192	94.1

Table 11 Economic and exergy parameters of components of the plant

Component	$\dot{E}x_f$ (kW)	$\dot{E}x_p$ (kW)	$\dot{E}x_d$ (kW)	$\dot{Z}_k$ ($/year)	r_k (%)
Turbine 2	189.5	164	25.5	2123	33.78
Condenser 1	26.53	9.305	17.22	1397	398.6
Pump 1	2.948	2.515	0.4828	1118	1049
HEX 1	454.4	213.6	240.9	2178	66
Turbine 1	146.6	127	19.4	153	18
Condenser 2	12.79	3.2	9.7	2924	436.2
Evaporator	23.45	8.38	15.07	10,658	354
LPA	57.34	4.096	53.24	7212	1705
HEX 2	14.39	11.1	3.292	20,577	0.1044
Pump 2	6.909	0.386	6.523	2047	40.52
LPG	124	96.86	27.17	7212	900
HPA	28.29	7.84	20.45	26,266	1290
Pump 3	2.37	0.06457	2.306	2047	569
HEX 3	12.97	8.977	3.995	1121	4.9
HPG	76.05	32.8	43.25	15,674	664.7
PEME	127	35.97	91.07	53.93	256

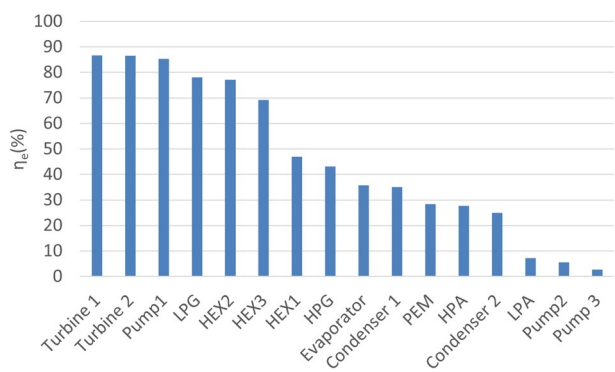

Fig. 3 Exergy efficiencies of components in the plant

Parametric study

The impact of the heat source temperature (T_7 or T_{HS}) on various parameters is shown in Fig. 4. At a geothermal heat source temperature of 100 °C, the flow delivered to the high-pressure generator of the absorption side has a low temperature of 50 °C, while the flow delivered to the low-pressure absorber is at 70 °C. As the temperature of HPG rises, $\dot{Q}_{HPG}$ and the temperature of vaporized water at line 35 also increases. However, there is a significant increase in h_{35}, which leads to a decrease in $\dot{m}_5$ to maintain energy balance, resulting in a decrease in $\dot{Q}_{ev}$. The decrease is about 10% at the end of the range. This behavior for half-effect absorption chillers is also reported in the literature for low generator temperatures (Gomri 2010). On the other hand, when the geothermal fluid temperature rises, the inlet enthalpy of turbine two also increases, resulting in a significant improvement in work output. In fact, by the end of the temperature range, the work output of turbine 2 becomes four times better than it was initially. A similar trend can be observed for hydrogen production, which utilizes the electricity generated by

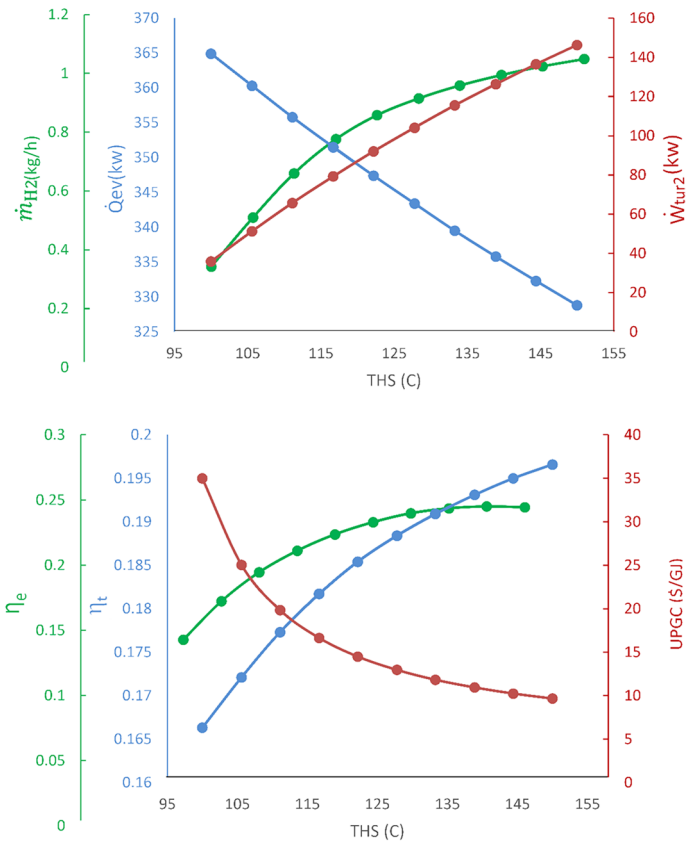

Fig. 4 Changes in several parameters with respect to geothermal flow temperature

turbine 1. As the geothermal fluid temperature increases, the hydrogen production rate also improves, and by the end of the temperature range, it becomes approximately 2.5 times greater than its initial value. With a rise in the hot water temperature, the UPGC decreases significantly, reaching one-third of its initial value by the end of the temperature range. Furthermore, both the exergy and thermodynamic efficiencies rise due to the hydrogen production rate and the work output from turbine 2.

The system is robust and can be easily adapted to operate with low-temperature resources. With a minor adjustment in the boundary conditions, it can be seen that according to Fig. 5, the system can effectively utilize resources with temperatures as low as 80 °C. It is important to note that during the energy transfer process to either turbine number one or the Rankine cycle, the temperature of the fluid decreases. For instance, when the resource temperature is 85 °C, the fluid temperature prior to the absorption chiller drops below 60 °C. In this temperature range, only a half-effect absorption chiller is capable of operating efficiently (Jayasekara and Halgamuge 2014).

The outlet pressure of turbine 1 is another significant parameter, as it impacts various system parameters (Fig. 6). As the outlet pressure increases, the work output delivered by turbine one decreases. Specifically, when the pressure is increased from 10 to 50 kPa, the hydrogen production rate decreases by approximately 12 times. This is anticipated because the power produced by this turbine is totally consumed by the hydrogen

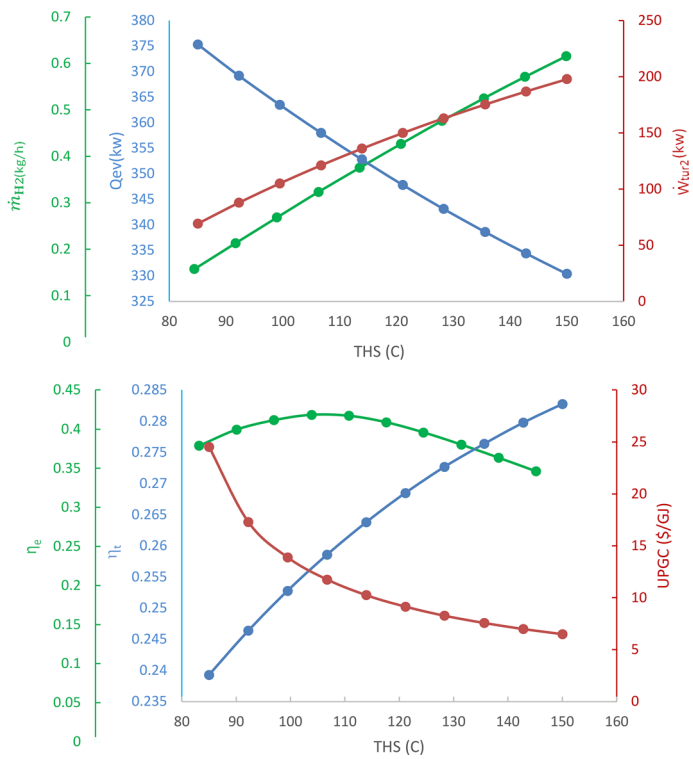

Fig. 5 Variation of selected parameters with respect to geothermal flow temperature (P_9(kPa) = 20 kPa and $T_5 - T_6 = 5^{oC}$)

production unit. However, the UPGC and the energy and exergy efficiencies do not change significantly with alterations in outlet pressure.

The intermediate pressure of the HEAC can affect the cooling process. It was the topic of some studies in the literature as researchers tried to find an optimal value for this parameter (Gomri 2011). The intermediate pressure in this study is defined as follows to investigate its influence on the performance of the system:

$$P_{26} = P_{38} + a \times (P_{35} - P_{38}).$$

Here, "a" is a dimensionless parameter between 0 and 1. In extreme conditions, when it is zero or one, P_{26} becomes P_{38} or P_{35}, respectively, and the absorption section becomes a single-effect absorption chiller (which is not the purpose of the current study). In other cases, P_{26} takes on a value between P_{38} and $P_{35,}$ and a half-effect absorption chiller exists.

Figure 7 illustrates the relationship between various parameters and the variable "a". Although there is an optimal value for both energy and exergy efficiencies at a specific "a" value, their variations with respect to "a" are not significant. Furthermore, the heat transfer rate ($\dot{Q}_{ev}$) is nearly 10% higher at the optimal "a" value. However, altering "a" does not significantly affect UPGC, indicating that improving the cycle through this variation does not impose a significant extra expense.

The amount of water absorbed in the HPA may be affected by the temperature of the cooling water and the HPA itself. Figure 8 illustrates the impact of these parameters on UPGC and the evaporator heat transfer rate. The figure shows that there is an optimal

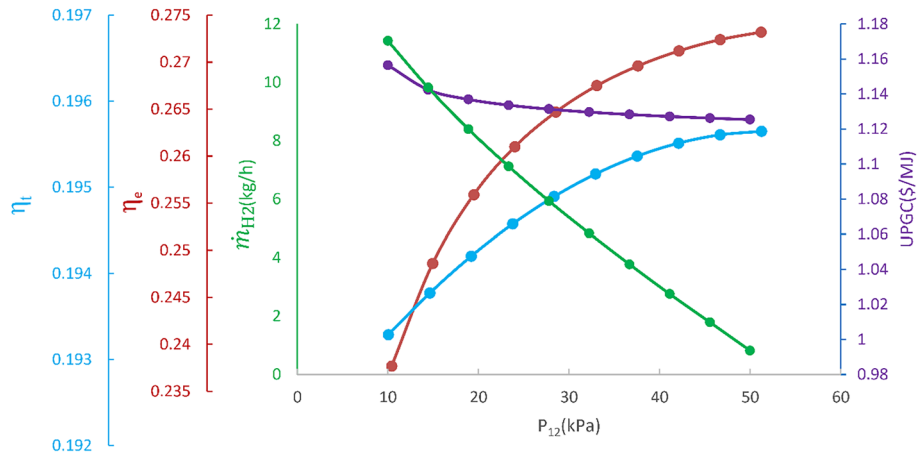

Fig. 6 Variation of several parameters with P_{12}

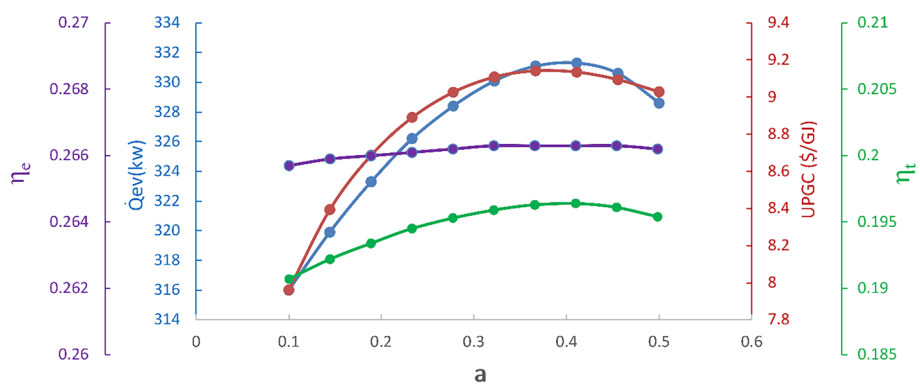

Fig. 7 Influences of "a" on several factors

value for both UPGC and $\dot{Q}_{ev}$, but the variations in their values are only around 2%, which is not considered significant.

The solution circulation ratio (also known as "*f*") is a fixed parameter in absorption chiller simulations that indicates the discrepancy between the concentration of the outlet and inlet flows from/to the vapor generators. It reflects the ability of the absorber and generators to absorb or generate vapor from brine effectively. This study considered a 5% difference in the beginning for this parameter. Figure 9 illustrates the influence of this parameter on the rate of heat transfer ($\dot{Q}_{ev}$) and UPGC on the high-pressure side (Δx_H). The figure shows that the solution circulation ratio significantly affects $\dot{Q}_{ev}$, while its impact on UPGC is not significant. This is because the element on that side mainly determines the concentration on the high-pressure side, and the concentration on the low-pressure side of the absorption chiller does not influence the overall performance significantly. Increasing the value of the solution circulation ratio decreases only UPGC because the need for a larger pump and heat exchanger on the low-pressure side is eliminated.

Improving the condensers as heat exchangers influences the overall efficiency and effectiveness of the plant. Figure 10 shows that increasing the temperature difference

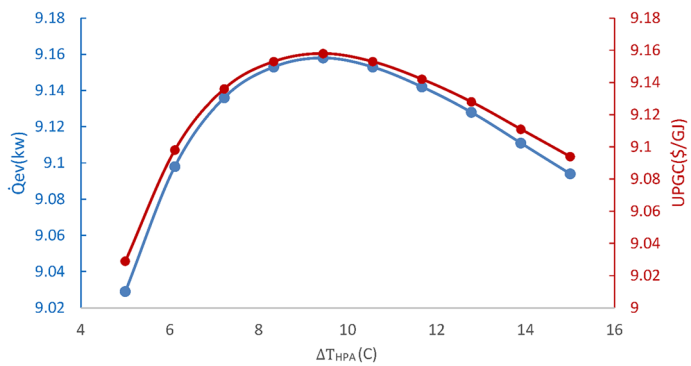

Fig. 8 Effects of temperature difference in HPA on the system performance

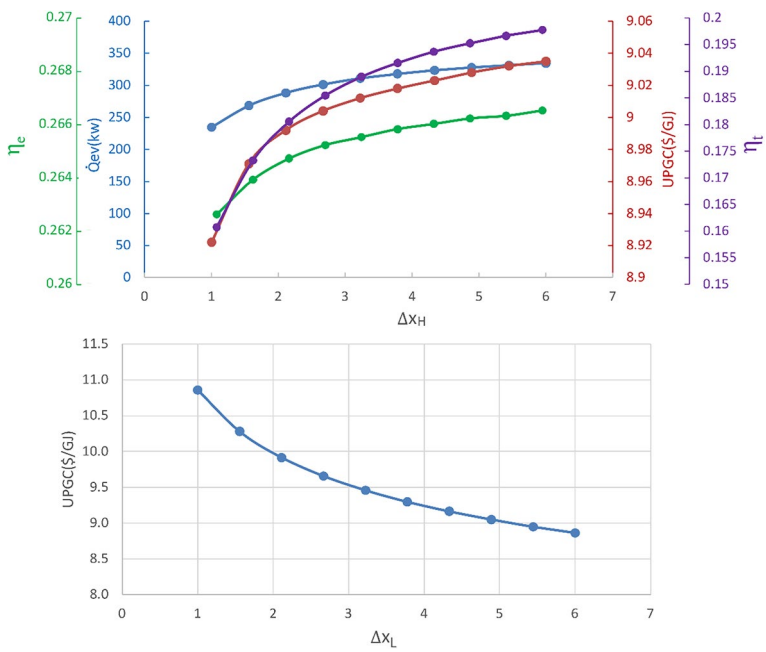

Fig. 9 Effects of Δx_L and Δx_H on several parameters

between the cooling fluid and the main flow in condenser two results in a decrease of approximately 5% in primary UPGC, while other parameters do not exhibit significant changes. However, the conditions differ in Condenser 1, where a 12 °C increase in temperature reduces values of all parameters other than UPGC by about 20%. The work delivered by turbine 2 decreases because of a higher exiting pressure. This directly affects the energy efficiency. Conversely, UPGC increases by about 18%.

The primary cause of exergy destruction in heat exchanger 1 of the ORC is the temperature difference between the working and cooling fluids. However, the mentioned temperature difference is intentionally set to obtain a higher temperature source for utilization in the cooling section. Figure 11 illustrates how this temperature difference affects various parameters. The data indicate that when the temperature difference in heat exchanger one rises, there is a corresponding increase in unit cost and a

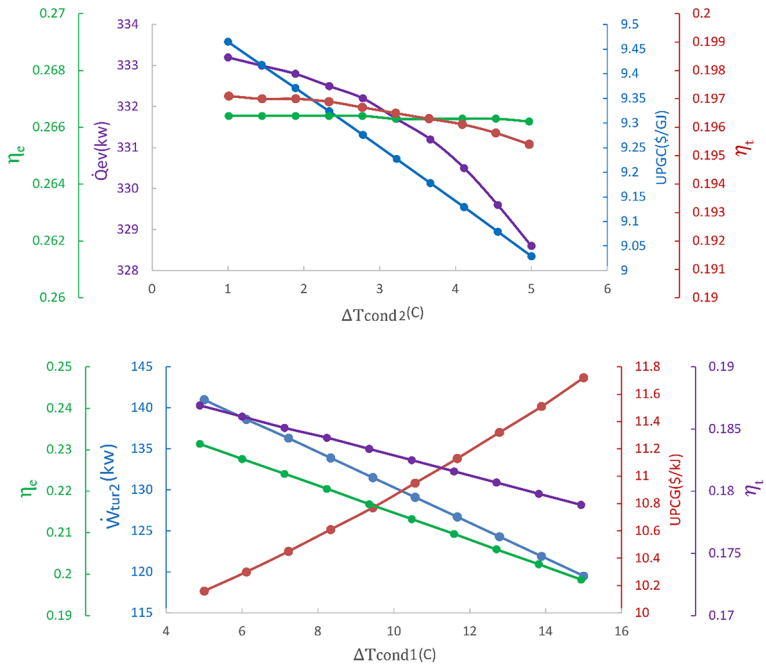

Fig. 10 Impacts of temperature difference in the condensers on the system's performance

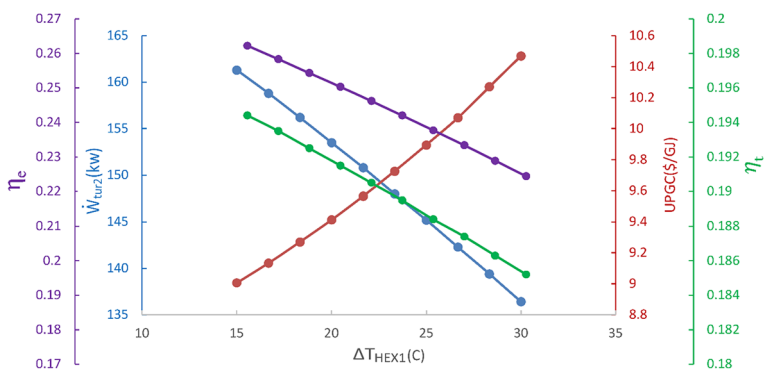

Fig. 11 Effects of temperature difference of HEX 1 on different factors

decrease in other parameters. Additionally, η_e decreases as the temperature difference increases. This suggests that it may be more beneficial to prioritize generating higher levels of electricity from turbine two instead of using the excess heat for cooling in the absorption chiller.

The system's performance can vary with different geothermal fluid mass flow rates (according to Fig.12). The results show that the system's exergy and thermal efficiencies decrease slightly as the flow rate rises while the hydrogen production rate improves. If all the generated electricity is consumed for producing hydrogen, a significant increase can be observed when the hot flow rate ($\dot{m}_7$) is increased to around 10 kg/s. However, the increase in hydrogen production becomes insignificant for further increases in the mass flow rate, indicating that exceeding this value is not economically feasible. Meanwhile, the heat transfer rate ($\dot{Q}_{ev}$) increases linearly with the mass

flow rate, implying that the system has better cooling performance at higher geothermal mass flow rates. If hydrogen production is not considered, the system's exergy and thermal efficiencies remain constant regardless of the mass flow rate of the geothermal fluid (Fig. 12).

Optimization

So far, it has been determined how much each factor contributes to the system's overall performance. An optimization process is required to achieve the best performance for the current system. Optimization typically involves identifying a problem's best solution while considering relevant conditions or limitations. In multi-objective problems, the objective function is a vector and a solution rarely optimizes all objectives simultaneously. Instead, there is a set of solution points, and trade-off answers are required. The NSGA-II method is faster than other ranking methods and uses a crowding distance to obtain a more uniform solution front. The crowding distance factor is used better to select solutions in terms of dispersion on one front (Thu Bui and Alam 2008). This algorithm is employed to optimize the current problem. The objective functions are UPGC and η_e. The decision factors and corresponding bounds are given in Table 12. There are ten decision variables. The Pareto front of the two objective functions is given in Fig. 13. All the points are optimal. The best point is A, which cannot be accessed practically. That is, the conflict between objective functions and the simultaneous finding of the minimum (optimum) values for both functions is impractical. When one objective function becomes a minimum, the other becomes a maximum, and vice versa.

There are two extreme conditions, points B and D. Exergy efficiency has the highest value at point D. It is about 50%, while UPGC is also high, which is undesirable. The exergy efficiency is about 30% at point B, but UPGC is as low as 3. A trade-off can be made. Assuming that both objective functions have the same weight, the Pareto front can be normalized to the range of 0 and 1. Then, the nearest point to point A can be found, which is point C. At this point, UPGC is about 4, and energy efficiency is 40%.

In Table 13, the current system configuration is compared with previously published designs, taking into account various performance parameters. Note that the compared designs have different layouts, working fluids, and overall purposes, which may influence their overall performances. However, by considering the available data, valuable insights can still be obtained. The current design (row 3 in the table) exhibits good performance in terms of hydrogen production and net power generation compared to the other designs. Note that while the study of Feili et al. (2020) achieves a higher thermal efficiency due to the inclusion of $\dot{Q}_{ev}$ in the numerator, the current study attains a higher overall exergy efficiency (η_e). Furthermore, it is worth considering the potential variations in system operation. If all electricity produced by the current study is utilized for hydrogen generation (row 4 in Table 13, Current study #2), the exergy efficiency decreases to 21%, but the hydrogen production rate increases significantly (by approximately 3.5 times). On the other hand, if all power is dedicated to electricity production (row 5 in Table 13, Current study #3) and the PEME is omitted, the thermal efficiency remains relatively unaffected, while the exergy efficiency rises to over 40%.

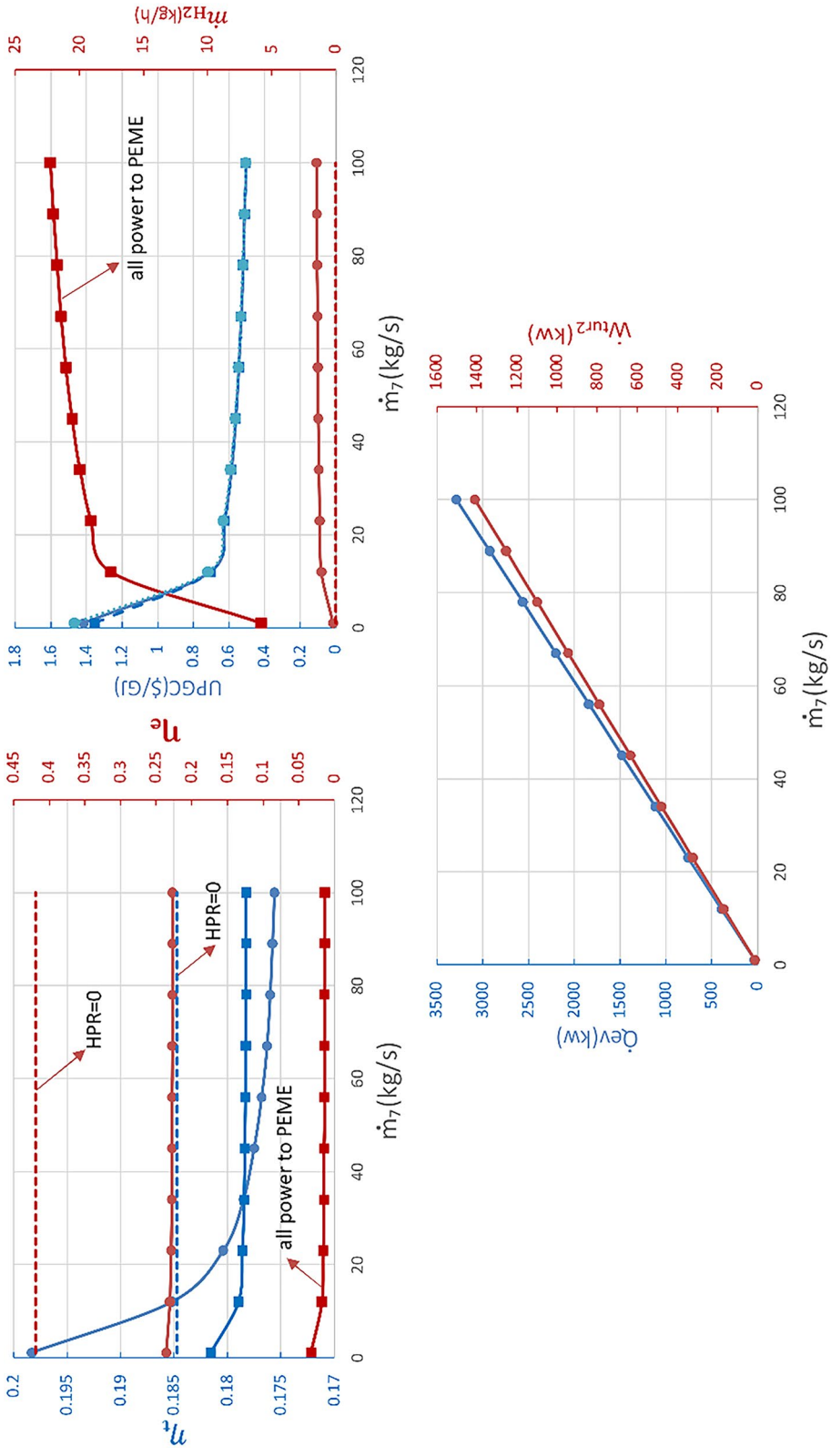

Fig. 12 Effects of hot source mass flow rate on various parameters

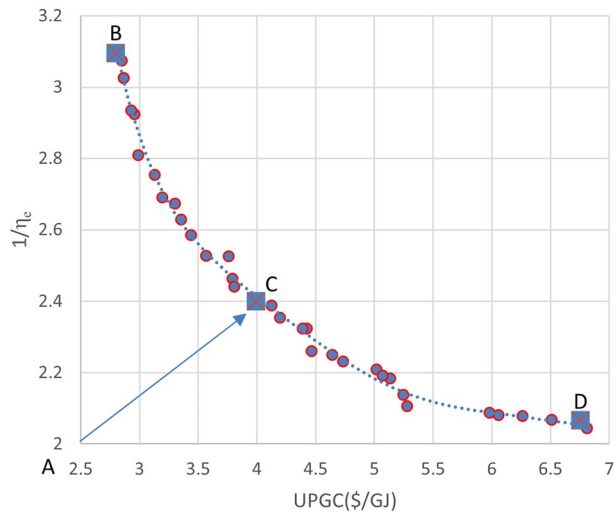

Fig. 13 Pareto front of the optimal points

Table 12 Decision variables and their bounds and optimal conditions

	Lower bound	Upper bound	B	D	C
T_7 (C)	100	170	165.85	112.44	139.06
P_9 (kPa)	10	30	27.66	26.75	26.86
a	0.1	0.5	0.33	0.28	0.22
ΔT_{HPA} (C)	5	10	8.01	6.23	5.98
Δx_H (C)	1	6	1.78	1.68	1.62
ΔT_{HEX1} (C)	14	35	24.73	14.27	14.89
$\dot{m}_5$(kg/s)	10	100	82.38	44.36	70.23
ΔT_{Cond1} (C)	1	10	2.63	1.40	1.28
ΔT_{Cond2} (C)	1	10	7.05	4.29	6.01
ΔT_{HS} (C)	1	20	1.95	2.10	2.24
η_e (%)			32.30	48.40	41.66
UPGC ($/GJ)			2.79	6.76	3.99
η_t (%)			25.99	26.03	25.77
$\dot{m}_{H_2}$(kg/s)			1.10	0.61	1.02

Table 13 Comparison of results from present work with those in the literature

	$\dot{m}_{HS}$ (kg/s)	T_{HS} (K)	T_0 (K)	$\dot{m}_{H_2}$ (kg/h)	$\dot{Q}_{ev}$ (kW)	$\dot{W}_{net}$ (kW)	η_t (%)	η_e (%)
Feili et al. (2020)	1.98	405	298.15	0.21	166.36	11.20	42.46	17.91
Azariyan et al. (2021)	1.98	405	298.15	0.30	45.57	16.23	19.35	20.95
Current study	1.98	405	298.15	0.72	67.5	28.96	27	35.7
Current study #2[a]	1.98	405	298.15	2.53	67.5	16	25	21
Current study #3[a]	1.98	405	298.15	0.014	67.5	34	27	43

[a] In #2, all of the power is used for hydrogen production. In #3, all of the power is delivered as electricity

Conclusion

Geothermal resources are available in various regions worldwide and offer a more consistent energy source than wind and solar energies. However, their relatively low temperature in many locations poses challenges for efficient utilization. This study explores implementing two systems, an ORC and a HERC, in conjunction with a PEME, to simultaneously generate electricity, cooling, and hydrogen from low-exergy thermal resources. The initial step involved a thermoeconomic evaluation of the system based on preliminary information and assumptions. The assessment demonstrated that the system can operate effectively even at low source temperatures. Under baseline conditions, the system yields 151.8 kW of power, 1.09 kg/h of hydrogen, and 328.6 kW of cooling. The system's energy and exergy energy efficiencies are approximately 19.5% and 26.5%, respectively. Next, the impact of several parameters on plant performance is assessed. An optimization process was then implemented to determine the optimal system performance. The optimization involved ten decision variables and utilized the NSGA-II algorithm to optimize conflicting parameters: unit polygeneration cost and exergy efficiency. The optimization results indicate that the system could achieve an exergy efficiency as high as 48.4%, with a thermal efficiency of 26.0% and a hydrogen production rate of 0.61 kg/h. In an alternative scenario, the system could produce 1.1 kg/h of hydrogen with an exergy efficiency of 32.0% and a thermal efficiency of 26.0%. The unit polygeneration cost for the first case is 6.76 $/GJ, and for the latter case is 2.8 $/GJ. Finally, a comparison was made between the performance of the base system and a similar plant discussed in the literature. The analysis indicated that the current system exhibits acceptable efficiency from a second-law perspective.

List of symbols

A	Area (m^2)
a	Parameter in pressure calculation of HEAC
c	Cost per unit exergy ($/GJ)
$\dot{C}$	Cost rate ($/h)
CRF	Capital recovery factor
D	Membrane thickness (μm)
E_{acta}	Anode activation energy (kJ/kg)
E_{actc}	Cathode activation energy (kJ/kg)
$\dot{E}x$	Exergy rate (kW)
$\dot{E}x_d$	Exergy destruction rate (kW)
f	Faraday constant (C/Mol)
h	Specific enthalpy (kJ/kg)
I_r	Interest rate (%)
J	Current density (A/m^2)
$J_{ref,a}$	Anode reference exchange current density (A/m^2)
$J_{ref,c}$	Cathode reference exchange current density (A/m^2)
k	Counter
LHV	Lower heating value (kJ/kg)
LMTD	Logarithmic mean temperature difference (°C)
$\dot{m}$	Mass flow rate (kg/s)
$\dot{m}_{H2}$	Hydrogen production rate (kg/h)
N	System lifetime (year)
P	Pressure (kPa)
P_0	Environmental pressure (kPa)
$\dot{Q}$	Heat rate (kW)
r	Relative cost difference
R	Characteristic gas constant (kJ/kg-°C)
R_{PEME}	Polymer electrolyte membrane resistance ($\Omega\ m^2$)
s	Specific entropy (kJ/kg-°C)
T	Temperature (°C, K)
T_0	Environmental temperature (°C)
THS	Temperature of heat source (°C)
U	Heat transfer coefficient (kW/m^2-K)

V	Voltage (V)
V_0	Reversible potential (V)
x	Concentration (%)
Z	Capital cost ($)
$\dot{Z}$	Capital cost rate ($/s)

Subscripts

0	Dead (environmental) state
a	Anode
act	Activation
c	Cathode
ch	Chemical
ev	Evaporator
F	Fuel
geo	Geothermal
H_2	Hydrogen
HS	Heat source
i	Counter (a, c)
in	Inlet
k	Kth component
ohm	Ohmic
out	Outlet
P	Product
p	Pump
q	Heat
tur	Turbine
w	Work

Abbreviations

Cond	Condenser
EV	Expansion valve
HEAC	Half-effect absorption chiller
HEX	Heat exchanger
HPA	High-pressure absorber
HPG	High-pressure generator
LPA	Low-pressure absorber
LPG	Low-pressure generator
ORC	Organic Rankine cycle
PEM	Proton exchange membrane
PEME	Proton exchange membrane electrolyzer

Greek letters

$\Delta T_{\text{Cond.1}}$	T_2–T_6 (°C)
$\Delta T_{\text{Cond.2}}$	T_{36}–T_{40} (°C)
ΔT_{HEX1}	T_9–T_4 (°C)
ΔT_{HPA}	T_{32}–T_{41} (°C)
ΔT_{HS}	T_7–T_8 (°C)
Δx_{H}	Solution concentration difference at high-pressure side (%)
Δx_{l}	Solution concentration difference at low-pressure side (%)
ε_{HEX}	Heat exchanger effectiveness
η_{e}	Exergy efficiency
η_{p}	Pump efficiency
η_{t}	Thermal (energy) efficiency
η_{tur}	Turbine efficiency
λ_{a}	Membrane anode surface water (1/Ω)
λ_{c}	Membrane cathode surface water (1/Ω)
$\lambda(x)$	Water content in the polymer
σ_{PEME}	Local ionic conductivity coefficient (s/m)
τ	Annual operation hours (h)
φ_{r}	Maintenance factor

Acknowledgements
Not applicable.

Author contributions
The authors confirm their contribution to the paper as follows: study conception and design: H-R Bahrami; analysis and interpretation of results: H-R Bahrami and M A Rosen; draft manuscript preparation: H-R Bahrami and M A Rosen. Both authors reviewed the results and approved the final version of the manuscript.

Funding
There has been no significant financial support for this work that could have influenced its outcome.

Availability of data and materials
Data available within the article (The authors confirm that the data supporting the findings of this study are available within the article).

Declarations

Competing interests
The authors declare that they have no known competing financial interests or personal relationships that could have appeared to influence the work reported in this paper.

Received: 12 October 2023 Accepted: 29 April 2024
Published online: 10 May 2024

References

Aghaziarati Z, Aghdam AH. Thermoeconomic analysis of a novel combined cooling, heating and power system based on solar organic Rankine cycle and cascade refrigeration cycle. Renew Energy. 2021;164:1267–83.
Aryanfar Y, Alcaraz JLG. Exergy and exergoenvironmental assessment of a geothermal heat pump and a wind power turbine hybrid system in Shanghai, China. Geothermal Energy. 2023;11:9.
Assareh E, Dejdar A, Ershadi A, Jafarian M, Mansouri M, Salek Roshani A, et al. Performance analysis of solar-assisted-geothermal combined cooling, heating, and power (CCHP) systems incorporated with a hydrogen generation subsystem. J Build Eng. 2023;65: 105727.
Aygun H. Investigation of exergetic and exergo-sustainability metrics for high by-pass turbofan engine at different power settings. Environ Prog Sustain Energy. 2021;40(6): e13700.
Azariyan H, Vajdi M, Rostamnejad TH. Assessment of a high-performance geothermal-based multigeneration system for production of power, cooling, and hydrogen: thermodynamic and exergoeconomic evaluation. Energy Convers Manage. 2021;236: 113970.
Bahrami HR, Fazli S. Comparative exergy and energy analyses of compression–absorption cascade refrigeration cycles with varied configurations and ejector implementations. In: Proceedings of the institution of mechanical engineers, 2024; Part E: Journal of Process Mechanical Engineering. p. 09544089241234121.
Balaji C. Thermal system design and optimization. Springer; 2021.
Balli O, Caliskan H. Various thermoeconomic assessments of a heat and power system with a micro gas turbine engine used for industry. Energy Convers Manage. 2022;252: 114984.
Blanke T, Hagenkamp M, Döring B, Göttsche J, Reger V, Kuhnhenne M. Net-exergetic, hydraulic and thermal optimization of coaxial heat exchangers using fixed flow conditions instead of fixed flow rates. Geothermal Energy. 2021;9:19.
Cao Y, Haghghi MA, Shamsaiee M, Athari H, Ghaemi M, Rosen MA. Evaluation and optimization of a novel geothermal-driven hydrogen production system using an electrolyser fed by a two-stage organic Rankine cycle with different working fluids. J Energy Storage. 2020;32: 101766.
Chakyrova D. Thermoeconomic analysis of biogas engines powered cogeneration system. J Thermal Eng. 2019;5(2):93–107.
Chen H, Li Z, Xu Y. Evaluation and comparison of solar trigeneration systems based on photovoltaic thermal collectors for subtropical climates. Energy Convers Manage. 2019;199: 111959.
Delpisheh M, Abdollahi Haghghi M, Mehrpooya M, Chitsaz A, Athari H. Design and financial parametric assessment and optimization of a novel solar-driven freshwater and hydrogen cogeneration system with thermal energy storage. Sustain Energy Technol Assess. 2021;45: 101096.
Domínguez-Inzunza LA, Sandoval-Reyes M, Hernández-Magallanes JA, Rivera W. Comparison of the performance of single effect, half effect, double effect in series and inverse absorption cooling systems operating with the mixture H_2O-LiBr. Energy Procedia. 2014;57:2534–43.
Doseva N, Chakyrova D. Energy and exergy analysis of cogeration system with biogas engines. J Thermal Eng. 2015;1(3):391–401.
Farajollahi A, Rostami M, Feili M, Ghaebi H. Thermodynamic and economic evaluation and optimization of the applicability of integrating an innovative multi-heat recovery with a dual-flash binary geothermal power plant. Clean Technol Environ Policy. 2023;25(5):1673–98.
Farshi LG, Mahmoudi SS, Rosen MA, Yari M, Amidpour M. Exergoeconomic analysis of double effect absorption refrigeration systems. Energy Convers Manage. 2013;65:13–25.
Feili M, Rostamzadeh H, Parikhani T, Ghaebi H. Hydrogen extraction from a new integrated trigeneration system working with zeotropic mixture, using waste heat of a marine diesel engine. Int J Hydrogen Energy. 2020;45(41):21969–94.
Florides GA, Kalogirou SA, Tassou SA, Wrobel LC. Design and construction of a LiBr–water absorption machine. Energy Convers Manage. 2003;44(15):2483–508.
Fu C, Shen Q, Wu T. Exergo-economic comparisons of solar cooling systems coupled to series/parallel absorption chiller types considering the lowest heat transfer area. Case Stud Thermal Eng. 2022;39: 102456.
Gholizadeh T, Vajdi M, Rostamzadeh H. Freshwater and cooling production via integration of an ethane ejector expander transcritical refrigeration cycle and a humidification-dehumidification unit. Desalination. 2020;477: 114259.
Gomri R. Performance analysis of low hot source temperature absorption cooling systems. Int J Ambient Energy. 2010;31(3):143–52.
Gomri R. Development of intermediate pressure correlation for the half-effect absorption cooling chiller. Int J Thermal Environ Eng. 2011;2(1):35–40.

Hai T, Radman S, Abed AM, Shawabkeh A, Abbas SZ, Deifalla A, et al. Exergo-economic and exergo-environmental evaluations and multi-objective optimization of a novel multi-generation plant powered by geothermal energy. Process Saf Environ Prot. 2023;172:57–68.
Hernández-Magallanes JA, Ibarra-Bahena J, Rivera W, Romero RJ, Gómez-Arias E, Dehesa-Carrasco U, et al. Thermodynamic analysis of a half-effect absorption cooling system powered by a low-enthalpy geothermal source. Appl Sci. 2019;9(6):1220.
Herold KE, Radermacher R, Klein SA. Absorption chillers and heat pumps. CRC Press; 2016.
Huang J, Abed AM, Eldin SM, Aryanfar Y, García Alcaraz JL. Exergy analyses and optimization of a single flash geothermal power plant combined with a trans-critical CO2 cycle using genetic algorithm and Nelder–Mead simplex method. Geothermal Energy. 2023;11:4.
Ioroi T, Yasuda K, Siroma Z, Fujiwara N, Miyazaki Y. Thin film electrocatalyst layer for unitized regenerative polymer electrolyte fuel cells. J Power Sources. 2002;112(2):583–7.
Jayasekara S, Halgamuge SK. A combined effect absorption chiller for enhanced performance of combined cooling heating and power systems. Appl Energy. 2014;127:239–48.
Karabuga A, Yakut MZ, Utlu Z. Assessment of thermodynamic performance of a novelty solar-ORC configuration based hydrogen production: an experimental study. Int J Hydrogen Energy. 2023;48(99):39154–68.
Khodaparast SH, Zare V, Mohammadkhani F. Geothermal assisted hydrogen liquefaction systems integrated with liquid nitrogen precooling; thermoeconomic comparison of Claude and reverse Brayton cycle for liquid nitrogen supply. Process Saf Environ Prot. 2023;171:28–37.
Li J, Zoghi M, Zhao L. Thermo-economic assessment and optimization of a geothermal-driven tri-generation system for power, cooling, and hydrogen production. Energy. 2022;244: 123151.
Loreti G, Facci AL, Baffo I, Ubertini S. Combined heat, cooling, and power systems based on half effect absorption chillers and polymer electrolyte membrane fuel cells. Appl Energy. 2019;235:747–60.
Marefati M, Mehrpooya M, Shafii MB. A hybrid molten carbonate fuel cell and parabolic trough solar collector, combined heating and power plant with carbon dioxide capturing process. Energy Convers Manage. 2019;183:193–209.
Maryami R, Dehghan AA. An exergy based comparative study between LiBr/water absorption refrigeration systems from half effect to triple effect. Appl Therm Eng. 2017;124:103–23.
Mohammadkhani F, Shokati N, Mahmoudi SMS, Yari M, Rosen MA. Exergoeconomic assessment and parametric study of a gas turbine-modular helium reactor combined with two organic Rankine cycles. Energy. 2014;65:533–43.
Mohseni M, Bahrami HR, Leili MS. Energy and exergy analysis of a steam power plant to replace the boiler with a heat recovery steam generator. Int J Exergy. 2024;43(1):1–20.
Nami H, Akrami E, Ranjbar F. Hydrogen production using the waste heat of benchmark pressurized molten carbonate fuel cell system via combination of organic Rankine cycle and proton exchange membrane (PEM) electrolysis. Appl Therm Eng. 2017;114:631–8.
Nami H, Ranjbar F, Yari M. Thermodynamic assessment of zero-emission power, hydrogen and methanol production using captured CO_2 from S-Graz oxy-fuel cycle and renewable hydrogen. Energy Convers Manage. 2018;161:53–65.
Nikam KC, Kumar R, Jilte R. Economic and exergoeconomic investigation of 660 MW coal-fired power plant. J Therm Anal Calorim. 2021;145(3):1121–35.
Pang KY, Liew PY, Woon KS, Ho WS, Wan Alwi SR, Klemeš JJ. Multi-period multi-objective optimisation model for multi-energy urban-industrial symbiosis with heat, cooling, power and hydrogen demands. Energy. 2023;262: 125201.
Putriyana L, Daud Y, Saha BB, Nasruddin N. A comprehensive data and information on low to medium temperature geothermal resources in Indonesia: a review. Geomech Geophys Geo-Energy Geo-Resour. 2022;8(2):58.
Razmi AR, Hanifi AR, Shahbakhti M. Design, thermodynamic, and economic analyses of a green hydrogen storage concept based on solid oxide electrolyzer/fuel cells and heliostat solar field. Renew Energy. 2023;215: 118996.
Safari F, Dincer I. Assessment and optimization of an integrated wind power system for hydrogen and methane production. Energy Convers Manage. 2018;177:693–703.
Schweigler C, Demmel S, Ziegler F. Single-effect/double-lift chiller: operational experience and prospect. In: Proceedings of the international sorption heat pump conference. 1999:533–9.
Shokati N, Ranjbar F. Thermodynamic and exergoeconomic analysis of combination of single-flash geothermal power cycle with Kalina and ORC with different organic fluids. J Solid Fluid Mech. 2015;5(1):177–92.
Singh OK, Kaushik SC. Thermoeconomic evaluation and optimization of a Brayton–Rankine–Kalina combined triple power cycle. Energy Convers Manage. 2013;71:32–42.
Tang X, Yan G, Abed AM, Sharma A, Tag-Eldin E, Aryanfar Y, et al. Conventional and advanced exergy analysis of a single flash geothermal cycle. Geothermal Energy. 2022;10:16.
Thu Bui L, Alam S. Multi-objective optimization in computational intelligence, theory and practice. IGI Global; 2008.
Toro C, Sciubba E. Sabatier based power-to-gas system: Heat exchange network design and thermoeconomic analysis. Appl Energy. 2018;229:1181–90.
Wang L, Bu X, Li H. Investigation on geothermal binary-flashing cycle employing zeotropic mixtures as working fluids. Geothermal Energy. 2019;5(7):36.
Wang D, Dahan F, Chaturvedi R, Almojil SF, Almohana AI, Alali AF, et al. Thermodynamic performance optimization and environmental analysis of a solid oxide fuel cell powered with biomass energy and excess hydrogen injection. Int J Hydrogen Energy. 2024;51:1142–55.
Wu H, Liu Q, Bai Z, Xie G, Zheng J. Performance investigation of a novel multi-functional system for power, heating and hydrogen with solar energy and biomass. Energy Convers Manage. 2019;196:768–78.
Yuksel YE, Ozturk M, Dincer I. Development and analysis of geothermal energy-based low-grade heat utilization in an integrated form for multigeneration with hydrogen. Sustain Energy Technol Assess. 2023;57: 103176.
Zare V, Takleh HR. Novel geothermal driven CCHP systems integrating ejector transcritical CO_2 and Rankine cycles: thermodynamic modeling and parametric study. Energy Convers Manage. 2020;205: 112396.

Zhang F, Yan Y, Liao G, Jiaqiang E. Energy, exergy, exergoeconomic and exergoenvironmental analysis on a novel parallel double-effect absorption power cycle driven by the geothermal resource. Energy Convers Manag. 2022;258: 115473.
Zhang K, Jiang S, Chen Z, Li H, Liu S. Geothermal development associated with enhanced hydrocarbon recovery and geological CO_2 storage in oil and gas fields in Canada. Energy Convers Manage. 2023;288: 117146.

Publisher's Note

Springer Nature remains neutral with regard to jurisdictional claims in published maps and institutional affiliations.